J. Fluid Mech. (2008), *vol.* 595, *pp.* 1–43.
doi:10.1017/S0022112007008567 Printed in the United Kingdom

Underwater sand bed erosion and internal jump formation by travelling plane jets

A. T. H. PERNG AND H. CAPART

Department of Civil Engineering and Hydrotech Research Institute,
National Taiwan University, Taiwan

(Received 15 October 2006 and in revised form 9 August 2007)

Theory and experiments are used to investigate the water and sediment motion induced along a sea bed by travelling plane jets. Steadily moving jets are considered, and represent an idealization of the tools mounted on ships and remotely operated vehicles (ROVs) for injection dredging and trenching. The jet-induced turbulent currents simultaneously suspend sand from the bed and entrain water from the ambient. To describe these processes, a shallow-flow theory is proposed in which the turbulent current is assumed stratified into sediment-laden and sediment-free sublayers. The equations are written in curvilinear coordinates attached to the co-evolving bed profile. A sharp interface description is then adopted to account rigorously for mass and momentum exchanges between the bed, current and ambient, including their effects on the balance of mechanical energy. Travelling-wave solutions are obtained, in which the jet-induced current scours a trench of permanent form in a frame of reference moving with the jetting tool. Depending on the operating parameters, it is found that the sediment-laden current may remain supercritical throughout the trench, or be forced to undergo an internal hydraulic jump. These predictions are confirmed by laboratory experiments. For flows with or without jump in which the current remains attached to the bed, bottom profiles computed by the theory compare favourably with imaging measurements.

1. Introduction

In estuarine, coastal and marine engineering, various underwater operations involve hydrodynamic action by tools that are moved steadily along the sea bed. Three examples are depicted in figure 1. Figure 1(*a*) shows a suction dredge, trailed behind a ship, used to extract sand from the bottom. For dense sands, jets may be mounted onto the suction head to loosen the soil prior to extraction (Zanker & Bonnington 1967). Another dredging technique which is entirely dependent on jetting action, called water injection dredging, involves trailing a multiport diffuser which discharges high-speed water onto the bed to entrain sediment into suspension (figure 1*b*). Provided that the sea bed is inclined, the suspended sand may then travel down the slope on its own in the form of a turbid plume (Knox, Krumholz & Clausner 1994).

A third task (figure 1*c*) has recently gained increasing importance owing to the development of offshore oil extraction and submarine transmission of power and data. The objective of this operation is to bury cables and pipelines under a protective layer of sand, of thickness of 1 or 2 m, in order to prevent damage by trailing anchors and fishing nets. Instead of performing the burial in two separate phases of excavation and backfilling, the operation is now often performed in a single pass using jet trencher

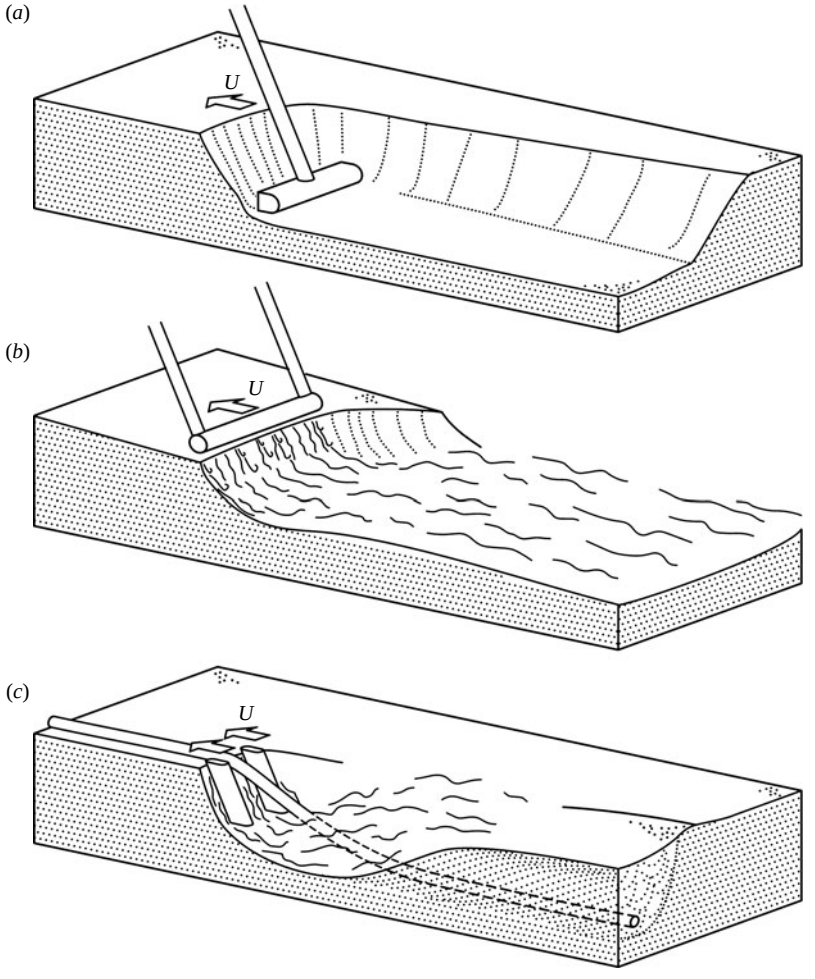

FIGURE 1. Erosion of underwater sand beds by steadily advancing tools, moved along the sea bottom using ships or remotely operated vehicles (ROVs): (*a*) suction dredging, in which sand is mined from the bed; (*b*) water injection dredging (after Knox *et al.* 1994), in which jetting is used to induce a turbid plume; (*c*) cable burial by jet trenching (based on information from Fugro Engineers), allowing the sand bed to be scoured and backfilled in a single pass.

ROVs (remotely operated vehicles). The 'product', cable or pipeline, is first simply laid onto the sea bottom. The vehicle then uses two upright or oblique swords lowered on both sides of the product to inject high-speed water into the sand bed. The jets scour a temporary trench, travelling with the vehicle, which allows the cable or pipeline to descend into the sea bed before being buried under the re-depositing sand further downstream of the trencher. Similar tasks have also been carried out using the suction hoppers of dredging ships (figure 1*a*), with the pumps operated in reverse to produce jets instead of suction (van Melkebeek 2002).

Although extensive testing and operational experience has been accumulated for jet trenching vehicles (see for instance Machin 2001), the flow processes involved are not yet well understood. Practical difficulties hindering such understanding include operation in difficult and turbid environments, as well as complicated patterns of water and sand motions.

Motivated by these practical applications and complications, an idealized variant of the jet trenching problem is examined in the present study. We consider the action of a travelling plane jet, moving steadily along an initially horizontal sediment bed composed of uniform sand. By neglecting transverse variations and assuming that the flow pattern has attained a steady state in a frame of reference attached to the jetting tool, the general unsteady three-dimensional flow will be reduced to a two-dimensional steady flow that is more readily amenable to theoretical and experimental study. Because actual jet trenching operations involve powerful jets acting on beds of relatively fine material (fine to medium sand), turbulent suspension will be the only sediment pick-up and transport mechanism considered. To document such flows, we will first present laboratory experiments conducted with carriage-mounted jets in a tank of constant width. With guidance from the experimental observations, a shallow-flow theory of the jet trenching process will then be proposed. The predictions of the theory will finally be checked against the laboratory measurements.

The erosional action of water jets impinging on submerged sediment beds has been examined in a number of previous studies. Pioneering work was conducted by Rouse (1940), who carried out flume experiments with downwards plane jets and examined how the style and pace of scour-hole development varied with jet strength and sediment characteristics. Over recent decades, extensive experimental work on erosion by fixed jets has been performed by Rajaratnam and co-workers (Rajaratnam 1981; Aderibigbe & Rajaratnam 1996; Mazurek, Rajaratnam & Sego 2003), who examined plane and circular jets impinging at various angles of attack onto beds composed of different sediment materials. For jet-induced scour limited by threshold-of-motion effects, theories have been proposed by Hogg, Huppert & Dade (1997), Gioia & Bombardelli (2005) and Bombardelli & Gioia (2006), and tested against laboratory experiments. Other related experiments include those of Mohamed & McCorquodale (1992), Stein, Julien & Alonso (1993) and Hopfinger *et al.* (2004). In all these works, the eroding jets were kept at a fixed position relative to the sand bed. In the present work, by contrast, we document the special phenomena arising when the jets travel along the bed. First, it becomes possible for the scour hole to attain a steady shape (in a frame of reference moving with the jetting tool) despite ongoing net erosion and deposition of sand across the loose bed interface. Secondly, different speeds of advance yield distinct patterns of flow and scour, including shooting flows with and without separation, as well as flows featuring an internal hydraulic jump. Finally, provided that the speed of advance is not too slow, the jet-induced water and sediment motions become sufficiently well-behaved to permit development of a hydraulic theory.

To describe theoretically the jet-induced current and the resulting sand erosion, suspension and deposition, we will rely both on shallow-water theory (see e.g. Abbott 1979) and work on turbulent entrainment (see e.g. Ellison & Turner 1959). To merge these avenues together, we will follow the roadmap laid out in a seminal paper by Parker, Fukushima & Pantin (1986). Based on the energy approach inaugurated by Bagnold (1966), Parker *et al.* showed that the influence of turbulence and erosion on the dynamics of gravity-driven turbidity currents could be described by shallow-flow equations, provided that one keeps track of the energy budget in addition to mass and momentum balance. A similar approach has been adopted by Kobayashi and co-workers (Kobayashi & Johnson, 2001; Kobayashi & Tega, 2002) to model suspended sediment transport in the coastal surf zone.

To describe the geomorphic turbidity currents induced by travelling jets, we must make various refinements to this basic theoretical approach. First, we will introduce a

sublayered description in which the turbulent bottom current is assumed stratified into sediment-laden and sediment-free sublayers. A generalization of the sharp interface view adopted by Fraccarollo & Capart (2002) will then be used to treat erosion and entrainment across the interfaces bounding these sublayers. Secondly, the steep trenching fronts obtained near the point of impingement will motivate the adoption of curvilinear coordinates. In similar contexts, such curvilinear coordinates have been used in two recent works to describe turbulent entrainment by curved jets (Jirka 2006) and basal erosion by shallow subaerial landslides (Chen, Crosta & Lee 2006). Finally, we will transform the governing equations to moving coordinates in order to describe the steady flows observed after long travel times in a frame of reference attached to the moving jets.

The paper is structured as follows. Section 2 describes the laboratory experiments performed to characterize jet trenching flows. In § 3, we derive our proposed sublayered shallow-flow equations. Section 4 is devoted to the construction of special travelling-wave solutions to these equations. The flow and solution details that must be addressed in order to compute long profiles of the bed and current are treated in § 5. Comparisons between computations and measurements are presented in § 6. Finally, conclusions are proposed in § 7.

2. Laboratory experiments

2.1. *Experimental apparatus*

To characterize the sand-bed response to the action of moving jets, small-scale experiments were performed at the Hydrotech Research Institute of National Taiwan University. The laboratory apparatus and procedure are shown in figure 2. Experiments take place in a rectangular tank having the following dimensions: length = 180 cm; height = 50 cm; inner width $B = 12.6$ cm. To obtain an unobstructed view, each sidewall is formed of a single glass panel of area 180 cm × 50 cm, with a thickness of 12 mm chosen to minimize deformation. The bottom of the tank is composed of an 18 cm thick layer of sand, submerged under a 29 cm deep clear-water ambient. Before each experiment, a scraping plate is used to give the sand surface a flat horizontal profile (dashed line in figure 2*a*). The level of the free surface of the water is kept constant during jetting by way of a siphon overflow. Photographs of the set-up are provided in Perng (2006).

The jetting device used to produce a plane jet is formed of three cylindrical jetting heads of width = 4.1 cm, placed side by side. Made of machined and welded copper, each head is supplied with high-pressure water (through a flexible polyurethane tube), and discharges the water at high speeds into the tank through a row of 19 nozzles of internal radius $R = 0.25$ mm. The resulting individual round turbulent jets can be expected to merge into a single uniform plane jet within distances of around 5 to 10 times the nozzle separation distance of 2 mm (Jirka 2006). The specific momentum flux per unit width of the corresponding equivalent plane jet is given by

$$\Sigma = hv^2 = \frac{Q^2}{BN\pi R^2}, \tag{1}$$

where $N = 3 \times 19 = 57$ is the number of nozzles, R their radius, B the channel width, and Q the total discharge fed to the jetting heads. The choice of three aligned but separate jetting heads is made to attain a more uniform spanwise distribution of jetting strength. In earlier tests, we found that we could not achieve the desired degree of uniformity with a single head spanning the entire tank width. The high-pressure

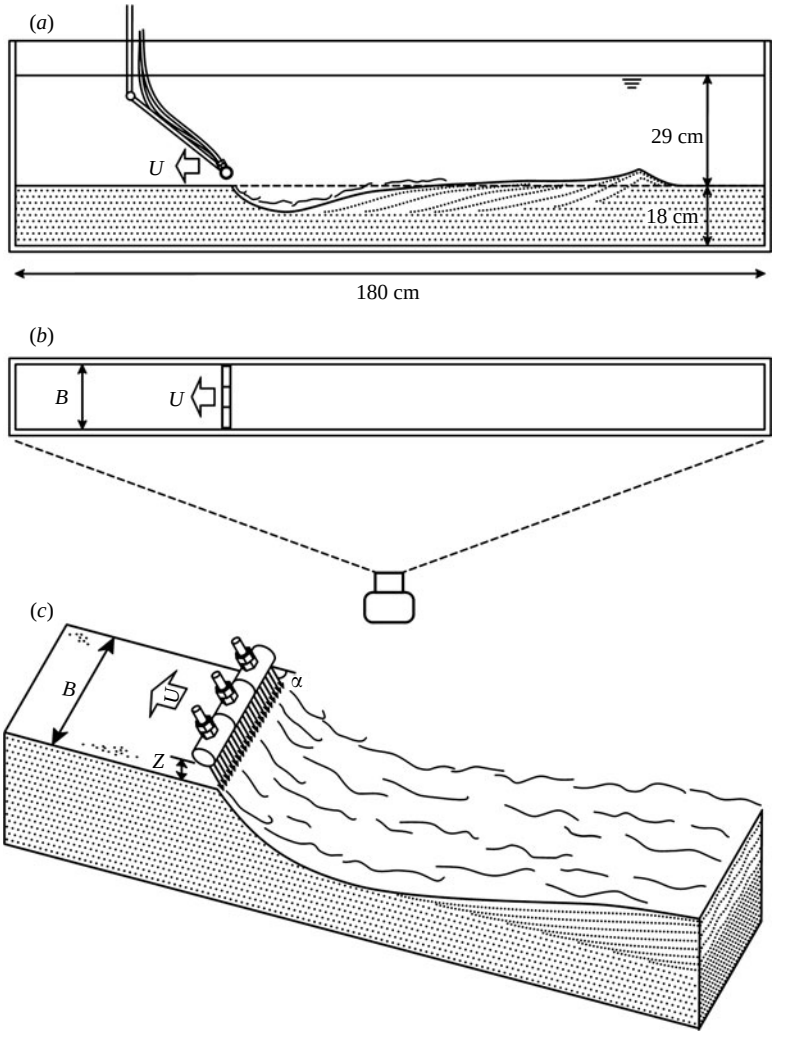

FIGURE 2. Experimental set-up: (*a*) side view of flume and moving jetting arm; (*b*) top view of flume and wide-angle camera used for time-lapse photography; (*c*) close-up of the travelling jetting heads and induced flow pattern.

water for the three heads comes from a three-way flow splitter, fed by a twin-piston irrigation pump. The pump is equipped with an air chamber to make the water supply very nearly steady, and its discharge can be adjusted to values up to $Q = 125\,\mathrm{ml\,s^{-1}}$.

To move the jetting device along the bed, a motor-driven traverse is placed above the tank, and travels at a constant speed U that can be set in the range $U = 1 - 10\,\mathrm{cm\,s^{-1}}$. The jetting device can also be held stationary ($U = 0$) to observe the sand-bed response to a fixed plane jet. An articulated arm mounted rigidly on the carriage is used to position the jets above the sand surface. The connection between the arm and the jetting tool is a three-degree-of-freedom wrist used to adjust the jetting orientation. Precise adjustment is required to achieve a laterally symmetric erosion pattern. A slight spanwise asymmetry of the impinging jets can be amplified by the eroding flow into a tilted sand surface of up to 30° sideways inclination. For all the experiments presented below, the jet orientation was set to $\alpha = 60°$, and the

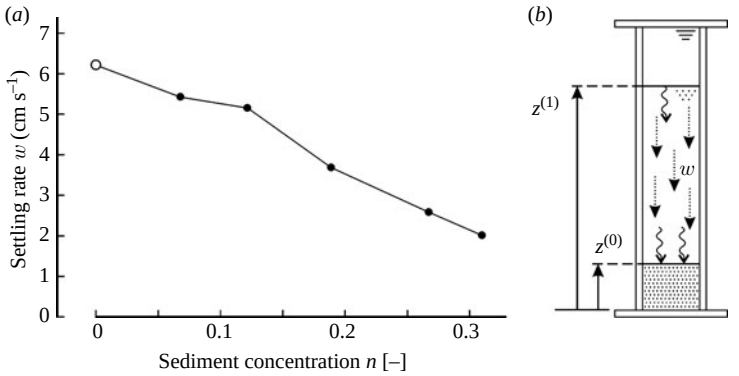

FIGURE 3. Sedimentation column tests: (*a*) measured settling rates $w(n)$ (filled circles) for various sediment concentrations n, compared with the fall speed $W = w(0)$ of individual sand grains (open symbol, mean of 20 measurements); (*b*) definition sketch. Tests performed in water near 30 °C.

standoff distance of the nozzles above the undisturbed bed was set to $Z = 5\,\mathrm{mm}$. Three jetting discharges $Q = 90$, 107 and $122\,\mathrm{ml\,s^{-1}}$ were examined. This corresponds to water velocities at the nozzles of 8.0, 9.6 and $10.9\,\mathrm{m\,s^{-1}}$, respectively, and to jetting strengths $\Sigma_1 = 5.81\,\mathrm{s^{-2}}$, $\Sigma_2 = 8.11\,\mathrm{s^{-2}}$, and $\Sigma_3 = 10.61\,\mathrm{s^{-2}}$. For each discharge, tests were performed at various speeds of advance U. Further tests conducted with another standoff distance $Z = 10\,\mathrm{mm}$ are described in Perng (2006).

2.2. *Sand properties*

The sand material used for the tests is a medium quartz sand of density $\rho_S = 2670\,\mathrm{kg\,m^{-3}}$, median diameter $d_{50} = 0.33\,\mathrm{mm}$, and coefficient of uniformity $d_{60}/d_{10} = 2.0$. The volumetric sand concentration in the static sedimented bed is estimated to be in the range $0.58 < n_0 < 0.62$. The settling of sand grains is known to depend on the concentration of the suspension (Richardson & Zaki 1954; van Rijn 1984). Measurements of fall speed and settling rates were therefore conducted at various concentrations (figure 3). Fall speeds are measured by timing the fall of individual sand grains between two horizontal lines, whereas settling rates are measured using sedimentation column experiments (figure 3*b*). For each concentration n, a known volume of sand is thoroughly mixed with water in a closed column, then left to settle under the action of gravity. Assuming that both the bed surface and turbid interface behave like kinematic shocks (see Ungarish 1993), their elevations $z^{(0)}$ and $z^{(1)}$ will change at rates governed by

$$\frac{\mathrm{d}z^{(0)}}{\mathrm{d}t} = \frac{nw}{n_0 - n}, \tag{2}$$

$$\frac{\mathrm{d}z^{(1)}}{\mathrm{d}t} = -w, \tag{3}$$

where $w = w(n)$ is the settling rate at the given concentration. The settling process leaves both the suspended sediment concentration n and the total sediment volume $n_0 z^{(0)} + n h_1$ unchanged. In the actual sedimentation column tests, only the bed interface $z^{(0)}$ is sufficiently sharp to be identified precisely. We therefore estimate the settling rate $w(n)$ from the formula

$$w(n) = \frac{n_0 - n}{n} \frac{\mathrm{d}z^{(0)}}{\mathrm{d}t}, \tag{4}$$

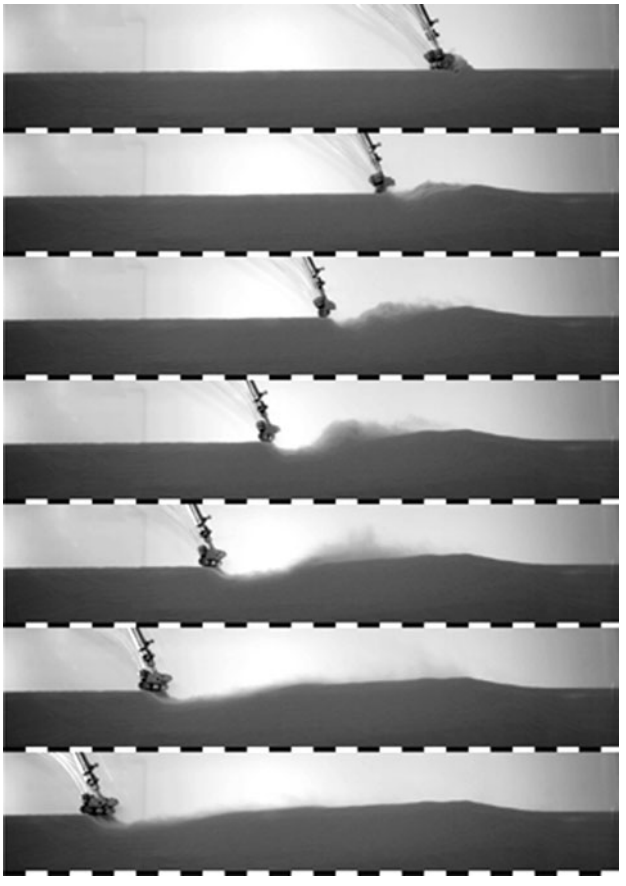

FIGURE 4. Time-lapse images of a jet trenching experiment from start-up (top panel) until approximate convergence to a moving trench of permanent shape (bottom panel). Successive panels are separated by intervals of 2 s. Each black or white segment of the scale bar is 5 cm long. Conditions for this test are $\Sigma = 8.11\,\mathrm{s}^{-2}$ (medium jetting strength) and $U = 6.8\,\mathrm{cm\,s}^{-1}$ (high speed of advance, leading to a shooting-flow pattern).

and time the rise of the sedimentation front $\mathrm{d}z^{(0)}/\mathrm{d}t$ either with a chronometer (for slower settling rates) or from time-lapse photographs (for higher sedimentation speeds). The resulting measurements are plotted in figure 3(*a*), with the mean fall speed of individual grains interpreted as the settling rate $w(0)$ in the dilute limit $n \to 0$. The deduced settling speed decreases with concentration as a result of hindered settling effects. The observed settling speeds range from $w(0) \approx 6\,\mathrm{cm\,s}^{-1}$ in the dilute limit to $w \approx 2\,\mathrm{cm\,s}^{-1}$ at concentration $n = n_0/2 \approx 0.3$.

2.3. *Experimental procedure and observations*

With reference to figures 2 and 4, moving jet experiments proceed as follows. The jetting tool is first positioned at one end of the tank, at the desired inclination and standoff distance above the horizontal bed. Carriage motion is then initiated, and shortly thereafter the pump is started. The ensuing bed erosion and sand suspension are observed through the tank sidewall. After travelling some distance along the bed, a stable flow pattern and scour-hole shape are established, and translate to the left with the jetting tool without significant further deformation. As required by conservation

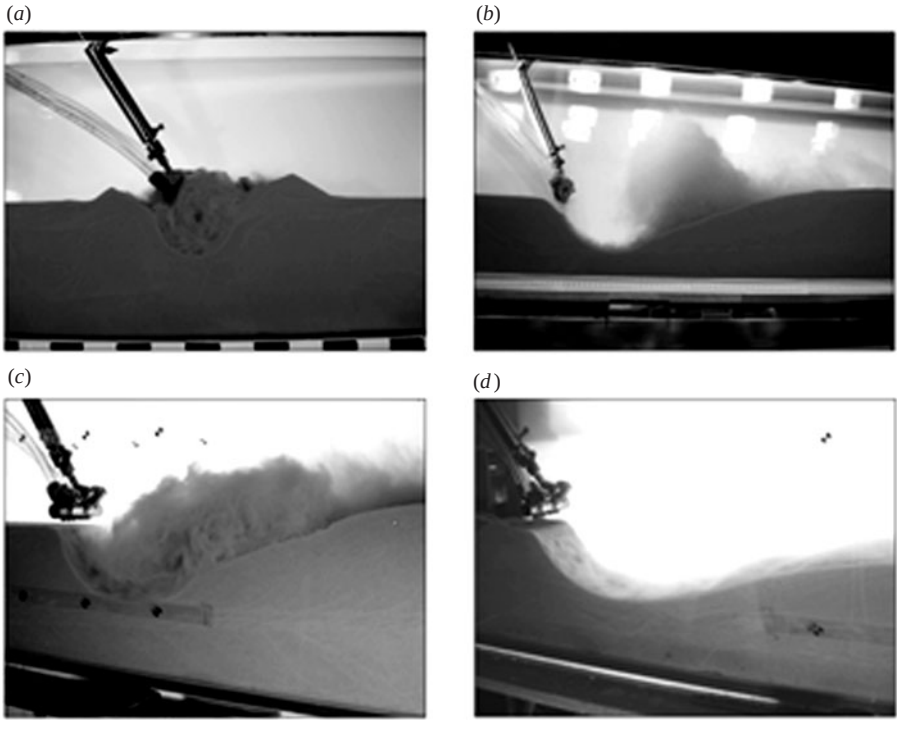

FIGURE 5. Qualitatively different flow patterns observed when varying the speed of advance of the plane jet relative to the sediment bed: (*a*) fixed jet; (*b*) very slowly moving jet; (*c*) slowly moving jet; (*d*) rapidly moving jet. The direction of the jet-induced current is from left to right in all cases, and the jetting tool translates from right to left in (*b*)–(*d*).

of sediment mass (neglecting variations in sedimented sand concentration before and after trenching), the scour hole travelling to the left leaves behind a sand heap in the start-up region, with equivalent positive and negative volumes on either side of the initial horizontal bed profile. The experiment ends as the jetting tool reaches the opposite end of the tank, when both the carriage and pump are stopped.

The different flow patterns produced when varying the speed of advance of the jetting tool relative to the sand bed are shown in figure 5. Our discussion here is qualitative, but a phase diagram will be presented in § 6.3 to delineate these various regimes in a more quantitative manner. To provide a point of reference, the flow observed when the jetting tool is held stationary is first presented in figure 5(*a*). In that case, sand eroded from the bed forms two triangular heaps on both sides of a stationary scour hole, attaining a steady shape in less than 1 min. Within this leveed scour hole, a mixture of sand and water circulates counterclockwise around a spanwise vortical axis. Clear water injected at high speed by the jetting head churns around then discharges to the ambient by detraining at low speed across a boiling turbid interface separating the turbulent suspension below from the clear water above. The observed pattern is similar to that documented by Rajaratnam (1981) in his early stationary plane-jet experiments. Unlike the threshold-of-motion conditions considered by Hogg *et al.* (1997) and Gioia & Bombardelli (2005), here the bottom of the scour hole attains a dynamic equilibrium in which turbulent entrainment of sand from the bed is balanced by gravitational settling of sand grains out of suspension.

When the jetting device is moved along the bed (figure 5*b–d*), the stationary sand heaps formed upon start-up are destroyed or left behind by the device and its associated travelling scour hole. Upon reaching steady state (in a frame of reference moving with the jetting head), qualitatively different flow and scour patterns are then obtained depending on the speed of advance. For very slow advance speed (figure 5*b*), the jet-induced turbulent current separates from the bed after deflection by the scoured profile. After flowing along the curved bed in the form of a thin bottom layer, the sediment-laden jet fountains upwards, then rains down its suspended sediment. This pattern is similar to the strongly deflected regime observed by Rouse (1940) in his experiments on unsteady scour by fixed jets. For the present case in which the jetting device is moving, another interesting feature can be observed ahead of the point of impingement of the jet with the bed (figure 5*b*). Significant deformation of the bed occurs owing to the formation of a breaching front. The jet-steepened sand slope relaxes back towards the angle of repose, through shallow avalanching that extends for some distance in front of the jet. Breaching processes of this kind have been described by Van den Berg, Van Gelder & Mastbergen (2002) and Mastbergen & Van den Berg (2003). Even though the angle of repose is exceeded at the trenching front, this breaching response is not observed for faster speeds of advance (figures 5*c*, *d*), possibly because it is delayed by granular dilatancy and its required water infiltration from the ambient.

Figure 5(*c*) shows the pattern observed when the jetting head is moved slowly instead of very slowly along the bed. Close to jet impingement, the thin current flows along a steep trenching front where sand material is being continuously eroded from the bed. As it reaches the deepest portion of the travelling trench, the bottom current then thickens dramatically, undergoing an internal hydraulic jump. Upon expanding, the suspended sand layer adopts a thickness that exceeds the scour depth, and experiences a corresponding sudden slowdown of the longitudinal flow velocity. At the sudden expansion, a strong counterclockwise circulation is observed in the upper portion of the current, with a smaller clockwise circulation bubble observed near the bed. These are the hallmark features associated with a strong internal hydraulic jump. Downstream of this jump, the flow gradually quietens down, with the suspended sand settling back to the bed in a manner reminiscent of settling column observations, with distance from the jump replacing time elapsed as the independent variable governing the pace of re-sedimentation.

Finally, as shown in figure 5(*d*), a fast speed of advance produces a more elongated scour hole, in which the turbulent current forms a shooting flow that simultaneously entrains water from the ambient and interacts with the underlying sand bed. The current is erosional along about a quarter of the trench length, then depositional for the remaining three-quarters, until the suspended sand has settled out and the bed has recovered its original elevation. All along this course, the suspended sand current remains confined to a thin layer flowing rapidly along the bed. For the experiments shown in figures 5(*b*) and 5(*d*), in which bed visibility is good, it can be checked that the bottom elevation of the trench is close to uniform in the spanwise direction. The same is true for the flows of figures 5(*a*) and 5(*c*) when the jets are stopped and visibility is regained. Whereas this may not be the case in other scour problems (Bombardelli & Gioia, 2006), three-dimensional wall effects do not appear to influence the bed shape significantly in the present experiments.

For stationary jet conditions such as those of figure 5(*a*), it is clear that a prediction of the jet-induced vortical flow, entrainment and detrainment would require some rather elaborate computational modelling. As in the approach of Gioia & Bombardelli

(2005), probably the best that could be expected from a simplified theory would be to obtain basic scaling relations between the jetting strength and the dimensions of the scour hole, to be compared with empirical scaling relations such as those obtained by Rajaratnam (1981). Likewise, the complicated flow pattern of figure 5(*b*), where both breaching and flow separation are observed, appears to lie beyond the reach of a simple theory. The situation is more favourable, however, for the conditions of figures 5(*c*) and 5(*d*), where the flow appears sufficiently well-behaved to permit a hydraulic theory of the interaction between jet, ambient and sediment. In what follows, we restrict our attention to these two regimes, which also correspond to the conditions of practical interest in jet trenching applications.

2.4. *Profile measurements*

As shown in figure 6(*a*), time-lapse photographs like those shown in figure 4 are used to extract longitudinal flow profiles. The photographs are taken using a low-distortion wide-angle lens, capturing the entire tank length, and oriented with the image plane parallel to the tank walls. Image acquisition is performed at the rate of one image per second. To obtain quantitative measurements, profiles are extracted from these images using manual mouse clicks, then converted to physical coordinates using a calibrated scale factor and rotation adjustment. Coordinates in the travelling frame of reference are obtained by measuring distances with respect to a moving origin chosen as the position of the nozzle closest to the sidewall, projected vertically down onto the initial sediment bed profile.

As illustrated in figure 6(*a*), two profiles are extracted from each image. The first is the bed profile (filled circles), separating the motionless sand deposit below from the flowing current above. As for the settling column tests, this boundary is rather sharp and its visual identification does not suffer from much ambiguity. The second profile extracted (open circles) is an upper boundary of the zone occupied by suspended sediment. As seen in figures 4 and 6(*a*), this transition between sediment-laden and sediment-free regions is reasonably sharp in some places, but rather diffuse in others, leaving ample room for the subjectivity of the analyst. This second profile should therefore be taken as indicative only.

To gauge the rate of convergence of the trench profile towards a steady shape in the travelling frame of reference, the bed profiles corresponding to the time-lapse images of figure 4 are plotted together in figure 6(*b*). For clarity, the profiles are distorted vertically by a factor of 2, and plotted in the moving coordinates. They are observed to converge rather rapidly towards a steady-state limit, the more so for positions located closer to the jetting tool. Convergence is slowest for the far end of the trench, where bed levels exceed the initial bed elevation as a result of the start-up heap, which requires a significant travel distance to be left behind. With the exception of the distal tail, where profiles may not be fully converged, profiles captured near the end of a run are thus checked to approximate an asymptotic steady shape, and will be used in § 6 for quantitative comparisons with steady calculations.

2.5. *Simple model and characteristic parameters*

Before developing a more complete theory, it is useful to sketch a simple model which explains how moving jets lead to the formation of a steady scour profile in a travelling frame of reference. Let $z^{(0)}$, h and u denote, respectively, the bed height, current thickness and longitudinal current speed along the curved profile of a shallow

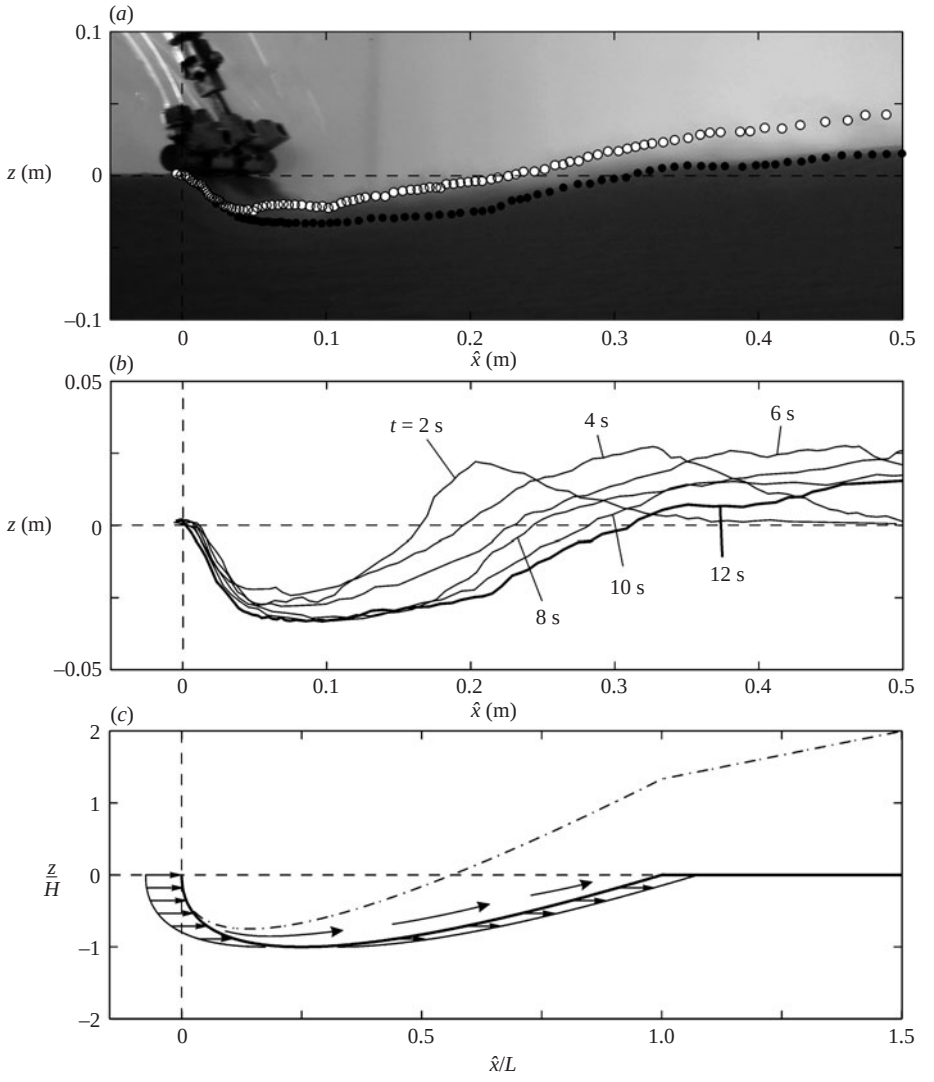

FIGURE 6. Longitudinal profiles: (*a*) bed profile (filled circles) and outer limit of suspended sediment (open circles) acquired manually from a digital image (time $t = 12\,\mathrm{s}$); (*b*) successive unsteady bed profiles (thin lines), converging towards a permanent shape approximated by the last profile (thick line) near the end of the experiment (vertical scale distorted by a factor of 2); (*c*) bottom profile (thick line) and current boundary (dash-dotted line) from a simplified model of the jet trenching process. Arrows indicate steady sand fluxes as perceived in a frame of reference moving with the jetting head.

trench. A simple unsteady equation for the local bed evolution can be written

$$\frac{\partial z^{(0)}}{\partial t} \approx -Eu + DW, \tag{5}$$

where E is a dimensionless erosion coefficient, D is a dimensionless deposition coefficient, and $W = w(0)$ is the fall speed in the dilute limit, all assumed constant for simplicity. At steady state in a frame of reference moving with the jetting tool (at

speed of advance U from right to left), the profile $z^{(0)}(x,t)$ reduces to $z^{(0)}(\hat{x})$ where

$$\hat{x} = x + Ut. \tag{6}$$

It follows that

$$\frac{\partial z^{(0)}}{\partial t} = \frac{\mathrm{d}z^{(0)}}{\mathrm{d}\hat{x}}\frac{\partial \hat{x}}{\partial t} = U\frac{\mathrm{d}z^{(0)}}{\mathrm{d}\hat{x}} = -Eu + DW, \tag{7}$$

which equates the flux of sand across the sloping bed surface to the rate of erosion and deposition by the jet-induced current. In figure 6(a), the thickness of the current is observed to vary roughly linearly with distance from the jetting head, i.e. $h \approx C\,\hat{x}$ where $C \approx 1/10$. If we assume that the momentum flux of the current $\Sigma = hu^2$ is approximately conserved as the current entrains bed material and ambient water, then $u(\hat{x}) \approx \sqrt{\Sigma / h(\hat{x})}$, and therefore

$$U\frac{\mathrm{d}z^{(0)}}{\mathrm{d}\hat{x}} = -E\sqrt{\frac{\Sigma}{C\,\hat{x}}} + DW, \tag{8}$$

which constitutes an idealized model of the trench response. The erosion rate is strongest near the jetting head and decays with distance, whereas the settling rate does not vary as long as suspended sand is available for deposition. The trench consequently deepens as long as erosion exceeds deposition, but rises back towards the undisturbed seabed level when settling starts to predominate. Neglecting the standoff distance between the jetting device and the sediment bed, this simple ODE can be solved immediately over the interval $0 \leqslant \hat{x} \leqslant L$ to yield

$$\frac{z^{(0)}}{H} = -4\sqrt{\frac{\hat{x}}{L}}\left(1 - \sqrt{\frac{\hat{x}}{L}}\right), \tag{9}$$

where

$$H = \frac{E^2}{CD}\frac{\Sigma}{UW}, \quad L = \frac{4E^2}{CD^2}\frac{\Sigma}{W^2} \tag{10}$$

are, respectively, the maximum depth and the length of the trench. The dimensionless profile obtained in this way is plotted in figure 6(*c*). The trench shape is asymmetric, with the point of maximum scour located at $\hat{x}/L = 1/4$, in qualitative agreement with the observed profile of figure 6(*a*). Approximate quantitative agreement for the trench depth and length for this and similar runs can be obtained by setting $D = 0.6$ and $E = 0.035$.

The above simple model and approximate coefficient values can be used to provide rough estimates of various characteristic parameters. The aspect ratio of the trench is for instance

$$\frac{H}{L} = \frac{D}{4}\frac{W}{U} \approx 0.15\frac{W}{U}, \tag{11}$$

suggesting that trenches become reasonably shallow once the speed of advance U exceeds the fall velocity W. At the location of deepest scour, furthermore, the current velocity u and friction velocity u_* are given by

$$u\left(\tfrac{1}{4}L\right) = \frac{D}{E}W, \quad u_*\left(\tfrac{1}{4}L\right) = \sqrt{f}\,u\left(\tfrac{1}{4}L\right), \tag{12}$$

where $f \approx 0.05$ is a bed friction factor (discussed further below). The corresponding ratio of friction velocity to fall velocity is then

$$\frac{u_*}{W} = \frac{D\sqrt{f}}{E} \approx 4. \tag{13}$$

This lies well beyond the suspension threshold $u_*/W = 1 - 1.25$ proposed by Bagnold (1966; see also Sumer *et al.* 1996). At such a high u_*/W value, the ratio of suspended load to total sediment load effectively reaches unity (see the experimental data of Guy, Simons & Richardson 1966; figure 18 in van Rijn 1984). Suspension-dominated transport can therefore be assumed, as confirmed visually by the photographs of figure 5. We can also gauge the relative magnitudes of the water velocity, speed of advance of the jetting head, and particle fall velocity. For the present experiments, the current velocity at the point of maximum scour is approximately $u(L/4) = DW/E \approx 1\,\mathrm{m\,s^{-1}}$. This is to be compared with speeds of advance U of the order of $5\,\mathrm{cm\,s^{-1}}$, and with water speeds through the jetting nozzles of the order of $10\,\mathrm{m\,s^{-1}}$. The velocity disturbance associated with the moving jetting head can therefore be safely neglected in comparison to the jet-induced water velocity. Likewise, the representative current velocity $u = 1\,\mathrm{m\,s^{-1}}$ (at the point of maximum scour) can be compared with the fall velocity $W = 6\,\mathrm{cm\,s^{-1}}$. As regards longitudinal flow motions, it therefore appears legitimate to treat the water–sediment mixture as a single phase (without interphase slip). For normal to bed motions, however, this is not the case, since the typical erosion speed (of the order of the jetting head speed at the trenching front) is of the same order as the fall velocity. Relative fluxes between the two phases must therefore be considered along the direction normal to the bed. Finally, for the test shown, maximum scour occurs approximately 10 cm away from the jetting head, or about 50 times the nozzle separation distance. While the round jets may not have merged completely before impinging with the bed, they can be expected to coalesce fully into a plane jet well before reaching the point of maximum scour.

These observations can be used to guide the formulation of a more complete theory, and overcome some key limitations of the simple model. It was assumed above that the coordinate $\hat{x}$ is equivalent to the distance travelled by the current. This approximation is reasonable for the shallowest trenches (such as the one shown in figure 6), but must be replaced by a curvilinear description for steeper trenching fronts such as those of figure 5(*c*) and 5(*d*). Most importantly, save for the settling of sand grains back to the bed, the simple model above does not account for gravitational influence. To deal with Froude-number effects (such as the formation of an internal hydraulic jump observed in figure 5*c*) and Richardson-number effects (the influence of density stratification on turbulence), a more elaborate theory is required and is developed in the next section.

3. Sublayered shallow-flow theory

3.1. *Notations and assumptions*

The various notations and assumptions used to derive the more complete theory are illustrated in figure 7. We consider the idealized situation sketched in figure 7(*a*). A plane jet submerged in a deep quiescent ambient impinges onto a loose stationary sediment bed, and we are interested in the ensuing pattern of water and sediment motion. Mean velocities are restricted to the x- and z-directions, and the flow is assumed uniform in the transverse direction. The jet-induced current takes the form of a turbulent bottom layer, flowing tangentially along the curved bed profile. Flow separation is not considered and the turbulent layer is assumed to remain attached to the stationary bed. Mass transfers occur both through the upper and lower boundaries of the turbulent current: quiescent water is entrained from the above ambient, and sand grains are eroded from the underlying bed. Sediment transport is taken to occur

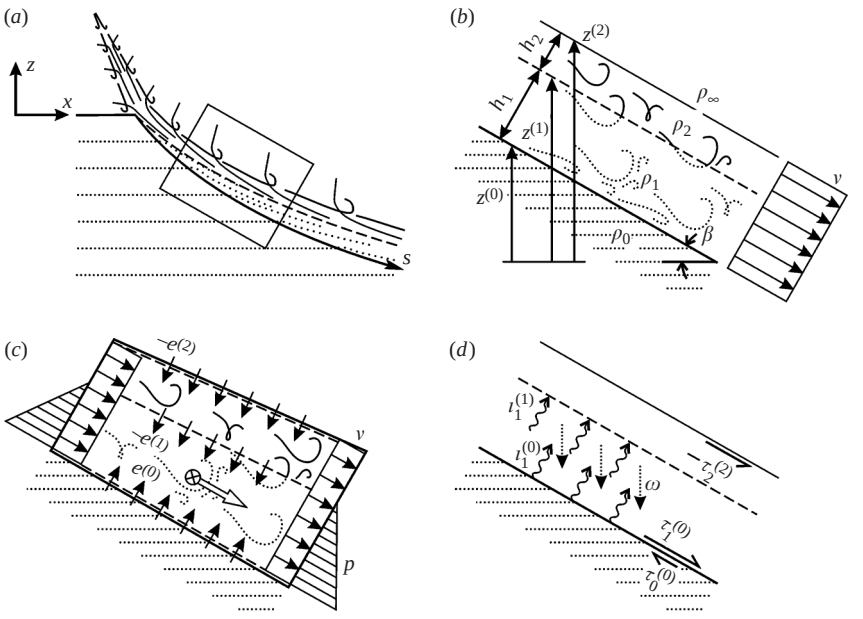

FIGURE 7. Flow idealization: (*a*) jet-induced turbulent current, assumed attached to the curved bed profile; (*b*) suspended sand sublayer embedded within the turbulent current; (*c*) control volume with longitudinal fluxes and interfacial transfers; (*d*) mass drift and shear stress functions.

as suspended load, with eroded sand grains eventually falling back to the bed by gravitational settling.

To model the above processes, a sublayered shallow-flow description is adopted. Because the bed profile may adopt a steep slope near the jet impingement, boundary-fitted coordinates are used. The curvilinear coordinate s denotes arclength along the bed. The bed profile $(x^{(0)}, z^{(0)})$ can then be integrated from

$$\frac{\partial x^{(0)}}{\partial s} = \cos\beta, \quad \frac{\partial z^{(0)}}{\partial s} = -\sin\beta, \tag{14}$$

where β is the local bed inclination below the horizontal. It is assumed that β is a slowly varying function of time and space, which can be considered constant on the scale of the adaptation time and length of the shallow current. Measured normal to the bed, the depth h of the flowing layer is considered small compared to the radius of curvature $\mathfrak{R}$ of the bed profile, i.e. $h \ll \mathfrak{R}$. The turbulent layer is further assumed to be sharply stratified into two distinct sublayers having depths h_1 and h_2, where $h_1 + h_2 = h$. The lower sublayer of depth h_1 is composed of a turbid mixture of turbulent water and suspended sand. The upper sublayer, on the other hand, features turbulent water taken to be entirely sediment-free. These two sublayers are distinguished in order to let turbulent water detrain from the turbid layer. As suggested by the experimental photographs of figures 4 and 5, the overall jet-induced turbulent layer of depth h can be expected to expand monotonously owing to mixing with the ambient, yet the thickness of its internal turbid layer h_1 will eventually decrease owing to the settling of sand grains. In addition to the bed profile $(x^{(0)}, z^{(0)})$, two other interfaces are therefore of interest: turbid interface $(x^{(1)}, z^{(1)})$ marks the limit between the sediment-laden and clear-water sublayers, and outer interface $(x^{(2)}, z^{(2)})$

denotes the limit between the turbulent current and the quiescent ambient. Their geometry is given by

$$x^{(1)} = x^{(0)} + h_1 \sin\beta, \quad z^{(1)} = z^{(0)} + h_1 \cos\beta, \tag{15}$$

$$x^{(2)} = x^{(0)} + (h_1 + h_2)\sin\beta, \quad z^{(2)} = z^{(0)} + (h_1 + h_2)\cos\beta. \tag{16}$$

Here and throughout the developments below, subscripts are used to denote layer quantities (e.g. the sublayer depths h_1, h_2), whereas superscripts denote interface quantities (e.g. the interface elevations $z^{(1)}$, $z^{(2)}$). A definition sketch is provided in figure 7(*b*).

Denoting by n_0 and n_1 the volume concentrations of sediment in the stationary bed and turbid sublayer, the densities of the bed, sublayers and ambient are

$$\rho_0 = \rho_W + n_0(\rho_S - \rho_W), \tag{17}$$

$$\rho_1 = \rho_W + n_1(\rho_S - \rho_W), \tag{18}$$

$$\rho_2 = \rho_\infty = \rho_W, \tag{19}$$

where ρ_W and ρ_S are the mass densities of water and sand, and where subscript ∞ is used to denote properties of the ambient. In what follows, the bed sand concentration n_0 and the densities ρ_0, ρ_2 and ρ_∞ will be assumed constant, but the sand concentration n_1 and the resulting density ρ_1 of the turbid sublayer will be allowed to evolve in time and space.

Contrasting with the stationary bed and quiescent ambient, the jet-induced turbulent current has a high velocity v, shared by the turbid and clear-water sublayers, and assumed to be oriented parallel to the local inclination of the stationary bed. The x- and z-components of the turbulent-layer velocity are thus approximated by

$$(u_x, u_z) = (v\cos\beta, -v\sin\beta). \tag{20}$$

Adopting a boundary-layer approximation, normal-to-bed components of the velocity will be disregarded in the balance of momentum and mechanical energy. This would not be valid for the stationary and very slowly moving jets of figures 5(*a*) and 5(*b*), where a two-dimensional roller and flow separation away from the bed are observed. For the slowly and rapidly moving jets of figures 5(*c*) and 5(*d*), however, the approximation appears reasonable since the flow direction is predominantly parallel to the bed.

3.2. *Governing equations*

As illustrated in figure 7(*c*), balance of volume, mass and momentum can be applied to control volumes wrapped around the whole turbulent layer or around each sublayer separately. Volume balance leads to the following continuity equations for the bed elevation $z^{(0)}$, and the depths h_1 and h_2 of the two sublayers:

$$\cos\beta\frac{\partial z^{(0)}}{\partial t} = -e^{(0)}, \tag{21}$$

$$\frac{\partial h_1}{\partial t} + \frac{\partial}{\partial s}(h_1 v) = e^{(0)} - e^{(1)}, \tag{22}$$

$$\frac{\partial h_2}{\partial t} + \frac{\partial}{\partial s}(h_2 v) = e^{(1)} - e^{(2)}. \tag{23}$$

In order to account for erosion and entrainment, terms $e^{(a)}$ on the right-hand sides denote volume transfer (per unit area) across interfaces $(x^{(a)}, z^{(a)})$, for $a = 0, 1, 2$,

respectively. Transfers are defined positive when volume is transferred from a lower layer to an upper layer. Conversely, transfers take negative values when volume goes from an upper layer to a lower layer, as expected for instance for turbulent entrainment from the outer ambient into the flowing current across interface $z^{(2)}$.

Because their mass densities remain constant, equations for the mass balance of the bed and sediment-free sublayers can be obtained simply by multiplying (21) and (23) by the corresponding densities ρ_0 and ρ_2. In the turbid layer, however, the sediment concentration and associated sublayer density can evolve. An additional equation for mass balance is thus required and can be written

$$\frac{\partial}{\partial t}(\rho_1 h_1) + \frac{\partial}{\partial s}(\rho_1 h_1 v) = i^{(0)} - i^{(1)}, \tag{24}$$

where the terms $i^{(a)}$, $a = 0, 1$, denote mass transfers across the corresponding interfaces. Again, mass transfers are defined positive when going up from a lower to an upper layer or sublayer. Two other useful equations can be obtained by linear combination of equations (21)–(24). The first is a balance equation for the overall mass $m = \rho_1 h_1 + \rho_2 h_2$ of the flowing layer (per unit bed surface):

$$\frac{\partial m}{\partial t} + \frac{\partial}{\partial s}(mv) = i^{(0)} - i^{(2)}, \tag{25}$$

where the mass flux $i^{(2)}$ across the outer interface is given by $i^{(2)} = \rho_2 e^{(2)}$. The second is a conservation equation for the total sediment mass

$$\frac{\partial}{\partial t}\{(\rho_0 - \rho_\infty) z^{(0)} \cos\beta + (\rho_1 - \rho_\infty) h_1\} + \frac{\partial}{\partial s}\{(\rho_1 - \rho_\infty) h_1 v\} = 0, \tag{26}$$

where the first term denotes the local rate of change of the sediment mass contained in both the bed and turbid sublayer, and the second term is the divergence of the turbid flux. In this equation, there are no non-conservative products on the left-hand side, and no source or sink terms on the right-hand side. It is the only one of the governing equations that can be cast in such a pure conservation form.

Because the two turbulent sublayers are assumed to share the same velocity v, a single momentum equation is needed, with only along-bed momentum considered. The corresponding balance equation is obtained for a control volume enclosing both sublayers jointly (figure 7*c*). Neglecting non-hydrostatic effects, momentum balance in the normal-to-bed direction reduces to an expression for excess pressure (relative to a sediment-free hydrostatic water column)

$$p(y) = \begin{cases} (\rho_1 - \rho_\infty) g \cos\beta (h_1 - y), & 0 \leqslant y \leqslant h_1, \\ 0, & h_1 < y, \end{cases} \tag{27}$$

where y is a local normal-to-bed coordinate, $p(y)$ is the local excess pressure, and g is the acceleration due to gravity. Including the thrust from these excess pressures, momentum balance in the along-bed direction s can be written

$$\frac{\partial}{\partial t}(mv) + \frac{\partial}{\partial s}\left\{mv^2 + \tfrac{1}{2}(\rho_1 - \rho_\infty) g \cos\beta\, h_1^2\right\} - (\rho_1 - \rho_\infty) h_1 g \sin\beta = j^{(0)} - j^{(2)}. \tag{28}$$

The terms on the left-hand side of this equation represent momentum change and flux, pressure thrust, and the along-bed component of the submerged weight. On the right-hand side, terms $j^{(0)}$ and $j^{(2)}$ represent momentum transfers across the lower and upper boundaries separating the turbulent current from its underlying sediment bed and outer ambient. Upwards transfers are again defined positive. Equations (21)–(28)

represent a generalization of the classical Saint Venant equations of open-channel hydraulics (see e.g. Abbott 1979). In the context of turbulent jets and boundary layers, the momentum equation equivalent to (28) is known as the von Kármán equation (see e.g. Mathieu & Scott 2000).

3.3. *Interface transfer relations*

Let $e(y)$ denote volume transfer across a line parallel to the bed at normal coordinate y. We decompose the mass transfer $i(y)$ across the same line as the sum of a convective transfer associated with e and a mass drift ι (iota) due to gravitational settling and correlated turbulent fluctuations:

$$i = \rho e + \iota, \tag{29}$$

where the mass drift can be written as Reynolds average $\iota = \langle \rho' u'_y \rangle$, in which ρ' and u'_y are local fluctuations in density and normal-to-bed velocity. Likewise, the normal-to-bed momentum transfer j is composed of a convective transfer associated with mass flux i combined with a shear stress τ:

$$j = v i - \tau, \tag{30}$$

where the minus sign before τ reflects the usual convention in which a positive shear stress drives a downwards flux of momentum. Expressed as a Reynolds average of correlated fluctuations of the parallel and normal to bed velocities u'_s, u'_y, the shear stress can be written $\tau = -\rho \langle u'_s u'_y \rangle$ for a homogenous fluid, with more complicated triple correlations arising in the presence of density fluctuations.

Across the interfaces $(x^{(a)}, z^{(a)})$ separating the flow sublayers from each other and from the bed and ambient, the quantities ρ, v, ι and τ may undergo discontinuous jumps. Notations $\iota_b^{(a)}$ and $\tau_b^{(a)}$ will be adopted to specify the mass drift and shear stress on side b of interface a. Consider first the bed interface $(x^{(0)}, z^{(0)})$. Turbulent suspension and gravitational settling drive a non-zero mass drift $\iota_1^{(0)}$ immediately above the interface on the side of sublayer 1. Underneath the interface, on the other hand, no mass drift occurs within the stationary sediment bed. Applied to an infinitely thin 'pillbox' control volume wrapped around the sharp interface, conservation of mass requires that the mass flux $i^{(0)}$ be the same on both sides, leading to the compatibility relation

$$i^{(0)} = \rho_0 e^{(0)} = \rho_1 e^{(0)} + \iota_1^{(0)}, \tag{31}$$

where ρ_0 and ρ_1 are the mass densities on both sides of the bed interface. Likewise, a turbulent shear stress $\tau_1^{(0)}$ will be applied on the top side of the bed interface, to which the stationary sediment bed below can oppose a resisting shear stress $\tau_0^{(0)}$. If the mass flux $i^{(0)}$ is non-zero, the two shear stresses will not be equal to each other. Instead, they must satisfy a second compatibility condition

$$j^{(0)} = -\tau_0^{(0)} = v i^{(0)} - \tau_1^{(0)}. \tag{32}$$

Here no convective term appears on the lower side of the interface because the velocity in the stationary bed is equal to zero. The two compatibility relations (31) and (32) are analogous to the Rankine–Hugoniot shock relations governing hydraulic jumps and bores. They represent a generalization of the morphodynamic interface relation used by Fraccarollo & Capart (2002) to relate erosion rate and shear stresses at the base of an erosional dam-break wave. In this earlier work, no mass drift was considered.

For interface $(x^{(1)}, z^{(1)})$ separating the turbid and clear-water sublayers, we have

$$i^{(1)} = \rho_1 e^{(1)} + \iota_1^{(1)} = \rho_2 e^{(1)}, \tag{33}$$

where mass drift is absent on the right-hand side because of the assumption that the top sublayer is entirely sediment-free. Because the two sublayers are assumed to share the same velocity v, no relation for the momentum flux $j^{(1)}$ is required. Finally, for interface $(x^{(2)}, z^{(2)})$ separating the turbulent layer and outer ambient, compatibility of the momentum flux requires

$$j^{(2)} = v i^{(2)} - \tau_2^{(2)} = 0, \tag{34}$$

where $i^{(2)} = \rho_2 e^{(2)} = \rho_\infty e^{(2)}$ and where $\tau_2^{(2)}$ is the turbulent shear stress applied below the interface. There is no mass drift on either side because both the upper sublayer and outer ambient are composed of water alone. Furthermore, the right-hand side of (34) is zero because the outer ambient is assumed to be devoid of both current and turbulence. The mass drift and shear-stress functions discussed above are illustrated in figure 7(*d*).

The balance equations and interface relations can be combined to obtain two additional equations that will be useful for the calculations below. The first is an evolution equation for the mass density of the turbid sublayer

$$\frac{\partial \rho_1}{\partial t} + v \frac{\partial \rho_1}{\partial s} = \frac{\iota_1^{(0)} - \iota_1^{(1)}}{h_1}, \tag{35}$$

which takes the form of an advection-source equation, where the source function is associated with mass drifts at the top and bottom of the sublayer. The second equation is an equation of motion for the turbulent layer:

$$\frac{\partial v}{\partial t} + v \frac{\partial v}{\partial s} + \frac{(\rho_1 - \rho_\infty) g h_1}{m} \frac{\partial z^{(1)}}{\partial s} + \frac{\frac{1}{2} g \cos\beta \, h_1^2}{m} \frac{\partial \rho_1}{\partial s} = \frac{-\tau_1^{(0)} + \tau_2^{(2)}}{m}, \tag{36}$$

where the right-hand-side sink term involves two shear stresses: the free-shear turbulent shear stress $\tau_2^{(2)}$ acting along the inner side of the upper boundary of the turbulent current, and the wall shear stress applied along the upper side of the erodible bottom $\tau_1^{(0)}$ (see figure 7*d*).

3.4. *Mass drift and shear stress functions*

Up to this point, the balance equations (21)–(28) and compatibility relations (31)–(34) are direct consequences of our basic assumptions, combined with conservation principles. To complete the description, however, it is necessary to provide semi-empirical laws for the turbulent mass drift and shear stress functions. For the mass drift functions, we adapt the classical sediment suspension theory of Rouse (1937) and write

$$\iota_1^{(0)} = \xi \sqrt{k} (\rho_0 - \rho_1) - (\rho_1 - \rho_\infty) \omega \cos\beta, \tag{37}$$

$$\iota_1^{(1)} = \xi \sqrt{k} (\rho_1 - \rho_2) - (\rho_1 - \rho_\infty) \omega \cos\beta, \tag{38}$$

where each drift function is expressed as the sum of an upwards turbulent diffusive flux and a downwards gravitational settling flux. The turbulent diffusive fluxes are assumed proportional to the square root of the specific turbulent kinetic energy k (per unit mass), multiplied by the density difference experienced across the corresponding interface. The non-dimensional proportionality constant ξ represents a ratio of eddy length l to shear-layer thickness δy, both assumed to scale with the depth h of the

turbulent layer. The downward gravitational drift, on the other hand, is expressed as the product of the local excess density with the normal-to-bed projection of the sediment settling rate ω. Because of hindered settling associated with the finite concentration of suspended sediment n_1 in the turbid layer, the effective settling rate ω will be lower than the fall speed of individual sand grains in unbounded fluid (Richardson & Zaki 1954). For the experiments described above, for instance, in which medium sand of diameter equal to 0.33 mm is used, the settling speed drops from $6\,\mathrm{cm\,s^{-1}}$ to $2\,\mathrm{cm\,s^{-1}}$ when the sand concentration goes from $n_1 = 0$ to $n_1 = 0.3$. Within this range, the effective settling speed that best accounts for the observed trench response is found to be $\omega \approx 3\,\mathrm{cm\,s^{-1}}$.

For the turbulent shear stress $\tau_1^{(0)}$ applied along the upper side of the stationary bed, we adopt the Chézy-type formula,

$$\tau_1^{(0)} = \rho_1 f |v| v, \tag{39}$$

applied by Kobayahsi & Johnson (2001) and Kobayahsi & Tega (2002) to the coastal surf and swash zones where fast water currents induce high rates of suspended sediment transport. For non-dimensional friction coefficient f, Raubenheimer, Elgar & Guza (2004) obtained values in the range 0.02–0.06 for beach uprush and downrush (Dronkers 2005). The friction coefficient f is known to be influenced by various processes, including the particle Reynolds number (Bombardelli & Gioia 2006), turbulence modulation due to the presence of solid grains (Crowe 2000), and sediment transport intensity (Wilson 1989; Sumer *et al.* 1996). For the present jet trenching conditions, however, the manner in which these processes should be jointly parameterized is unclear, and we choose instead a constant friction factor f to be tuned by comparison with the experiments. Towards the higher end of the range quoted above, value $f \approx 0.05$ is found to yield the best agreement and used for all the calculations reported below.

For the turbulent shear stress $\tau_2^{(2)}$ applied on the inner side of the outer interface, the situation is close to free-shear turbulence, and we adapt the turbulent stress function used in standard one-equation turbulence models (Fredsøe & Deigaard 1992). By analogy with the Kolmogorov–Prandtl eddy-viscosity expression $\nu_\mathrm{T} = l\sqrt{k}$, the shear stress function is written

$$\tau_2^{(2)} = \rho_2 \xi \sqrt{k}(-v), \tag{40}$$

where $-v$ is the velocity difference across the interface, and where non-dimensional parameter ξ is again the ratio of eddy length l to shear-layer thickness δy. Based on the assumption that the same turbulent eddies mix both momentum and density, the same constant ξ is used in (37), (38) and (40).

For the bed reaction shear stress $\tau_0^{(0)}$, there is no need for any additional empirical function. Combining the two compatibility functions (31) and (32), we obtain

$$\tau_0^{(0)} = \tau_1^{(0)} - \frac{\rho_0 v \iota_1^{(0)}}{\rho_0 - \rho_1}. \tag{41}$$

By Euler's momentum theorem, momentum transport associated with mass flux across the assumed infinitely thin interface is balanced by a jump in shear stress. In the absence of mass flux, this jump vanishes and the identity $\tau_0^{(0)} = \tau_1^{(0)}$ is retrieved in accordance with Newton's third law. The resisting shear stress on the lower side of the bed interface is therefore fully determined once the mass drift and shear stress functions $\iota_1^{(0)}$ and $\tau_1^{(0)}$ have been specified. We address in the next section the derivation

of an additional balance law for the evolution of the specific kinetic energy k of the turbulent velocity fluctuations, which intervenes in the three functions (37), (38) and (40).

3.5. *Balance of mechanical energy*

To close the description, energy balance must be invoked. The total mechanical energy of the system is composed of three different contributions: (i) the potential energy of the bed, current, and ambient system; (ii) the kinetic energy of the mean flow; (iii) the kinetic energy of the turbulent velocity fluctuations. For the latter, we do not distinguish between the solid and fluid phase, and consider the joint kinetic energy of the mixture. Approaches resolving the two phases separately have been proposed by Hsu, Jenkins & Liu (2003) and Ten Cate *et al.* (2004), but exceed the level of detail sought in the present work. Accordingly, the total energy flux across a vertical transect is due to advection of the different energy components complemented by the work of the excess pressure forces. The resulting balance equation is

$$\frac{\partial}{\partial t}\left\{\tfrac{1}{2}(\rho_0-\rho_\infty)g\,z^{(0)2}\cos\beta+(\rho_1-\rho_\infty)gh_1\left(z^{(0)}+\tfrac{1}{2}h_1\cos\beta\right)+\tfrac{1}{2}mv^2+mk\right\}$$
$$+\frac{\partial}{\partial s}\left\{\left[(\rho_1-\rho_\infty)gh_1\left(z^{(0)}+\tfrac{1}{2}h_1\cos\beta\right)+\tfrac{1}{2}mv^2+mk+\tfrac{1}{2}(\rho_1-\rho_\infty)g\cos\beta\,h_1^2\right]v\right\}=-\gamma, \tag{42}$$

where the first term on the left-hand side is the time rate of change of the total mechanical energy (sum of potential energy, mean flow kinetic energy, and kinetic energy of the turbulent fluctuations, per unit bed surface), and the second term on the left-hand side is the divergence of the energy flux. Note that the potential energy is measured with respect to a ground state in which the settled sea bed rises to elevation $z^{(0)}=0$ below a sediment-free water ambient. The symbol γ on the right-hand side of (42) is the energy dissipation function. Assuming an isothermal system, the second law of thermodynamics requires that this dissipation function be everywhere positive, i.e. $\gamma\geqslant 0$ (see e.g. Abbott 1979).

In order to obtain a balance equation for the kinetic energy of the fluctuations alone, we can form the quasi-linear combination

$$\text{(equation (42))}-\tfrac{1}{2}v^2\times(25)-mv\times(36)-\left\{(\rho_0-\rho_\infty)gz^{(0)}+(\rho_1-\rho_\infty)gh_1/\cos\beta\right\}\times(21)$$
$$-\left\{\tfrac{1}{2}(\rho_1-\rho_\infty)g\cos\beta\,h_1-\rho_\infty g\left(z^{(0)}+\tfrac{1}{2}\cos\beta\,h_1\right)\right\}\times(22)-g\left(z^{(0)}+\tfrac{1}{2}h_1\cos\beta\right)\times(24). \tag{43}$$

After repeated application of the chain rule, a considerable amount of algebra, and right-hand-side substitutions based on the compatibility relations (31)–(34), the resulting equation simplifies to

$$\frac{\partial}{\partial t}(mk)+\frac{\partial}{\partial s}(mkv)=\tfrac{1}{2}\left(\tau_0^{(0)}+\tau_1^{(0)}\right)v+\tfrac{1}{2}\tau_2^{(2)}(-v)-\tfrac{1}{2}g\cos\beta\,h_1\left(\iota_1^{(0)}+\iota_1^{(1)}\right)-\gamma, \tag{44}$$

which is one of the key results of the overall derivation. This equation is a balance law for the turbulence intensity k, where we recognize on the right-hand side the following source and sink terms. The first two terms are production terms associated with the work of the mean flow against the interfacial shear stresses $\tau_b^{(a)}$, and correspond to a loss of kinetic energy by the mean flow. The third term is a sink term associated with the work of the turbulent fluctuations against gravity, and corresponds to a gain of potential energy induced by the upwards mass drifts $\iota_b^{(a)}$. Finally, the last term is the energy dissipation function, inherited from the overall balance of mechanical

energy (42). It is seen from the right-hand side of (44) that both the production and gravitational work contributions are naturally expressed in terms of the shear stress and mass drift functions, further motivating our introduction of these terms.

In order to close the above cascade of equations, the final element that is required is a semi-empirical specification of the dissipation function γ. For this function, we adopt the formulation

$$\gamma = \tfrac{1}{2}\tau_0^{(0)} v + m\varepsilon + g\, h_1(\rho_1 - \rho_\infty)\omega(\cos\beta)^2, \tag{45}$$

similar to that proposed by Parker *et al.* (1986), and composed of the following three contributions. The first is a direct dissipation of the work of the shear stress $\tau_0^{(0)}$ applied to the lower side of the bed interface. Because this shear stress is only a reaction of the sediment bed, we expect the associated work to be dissipated locally rather than contribute to the production of turbulence. The second term represents the more standard dissipation of turbulent kinetic energy associated with transfer to smaller eddies and eventual dissipation by viscosity. This dissipation would occur even if settling sand grains were absent in the turbulent layer. Although the presence of sand particles may exert an influence on this term (Crowe 2000), we neglect it in first approximation. The third term, finally, is the Knapp–Bagnold dissipation introduced by Parker *et al.* (1986), and is associated with potential energy loss due to gravitational settling. This ongoing potential energy drop is not transferred back to the turbulence but rather lost to viscous processes.

For the rate of turbulent energy dissipation per unit mass ε, we adopt the standard expression

$$\varepsilon = c_2 \frac{k^{3/2}}{l}, \tag{46}$$

derived from the dimensional arguments of Kolmogorov (1941). Here l is again the eddy length (or length scale of turbulence), and c_2 is a non-dimensional constant. The standard $k-\varepsilon$ model value for this parameter is $c_2 \approx 0.08$, while the eddy length can be assumed to scale with the depth of the turbulent layer as $l \approx 0.1\, h$ (Fredsøe & Deigaard 1992). Like Hsu *et al.* (2003), we do not make corrections to these values owing to the presence of solid particles. We will thus model the rate of turbulent dissipation by the formula

$$\varepsilon = \chi \frac{k^{3/2}}{h_1 + h_2}, \tag{47}$$

where the non-dimensional constant χ takes the value $\chi = 0.08/0.1 = 0.8$.

Since h_1, $(\rho_1 - \rho_\infty)$, ω, k and ε are positive, both the Knapp–Bagnold and turbulent dissipation terms are automatically greater than or equal to zero. To guarantee overall dissipation, however, the first term must also be positive, i.e.

$$\tau_0^{(0)} v \geqslant 0, \tag{48}$$

which amounts to requiring that the bed reaction shear stress must oppose velocity v. By virtue of interface relation (41), this places a constraint on the maximum mass drift that can be attained near the bed:

$$\iota_1^{(0)} \leqslant \frac{\rho_0 - \rho_1}{\rho_0} \frac{\tau_1^{(0)}}{v}, \tag{49}$$

and this constraint will be enforced in the computations.

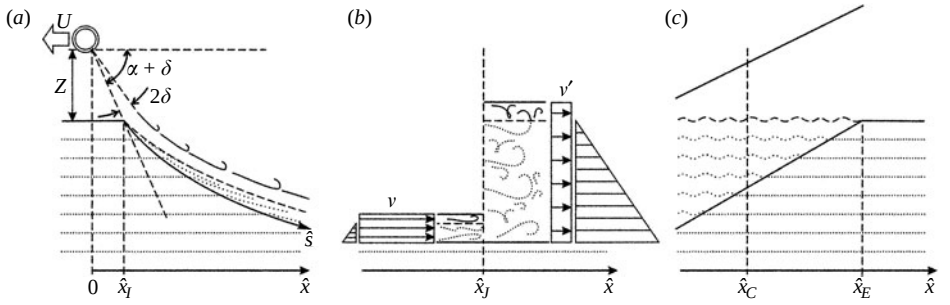

FIGURE 8. Flow details: (*a*) jet expansion before and after bed impingement; (*b*) internal hydraulic jump; (*c*) detrainment and settling pool.

4. Travelling-wave solutions

4.1. *Equations in moving coordinates*

We now consider the case of a plane jet travelling along an initially horizontal sea bed. Approximating a steadily advancing injection dredge or jet trencher (see figure 1*b*, *c*), the jetting device is assumed to move at constant speed U to the left. To describe the resulting water flow and sand bed response, it is then convenient to postulate an observer moving with the jetting device at the same leftward speed U. The corresponding change of independent variables $(x, t) \leftrightarrow (\hat{x}, \hat{t})$ is given by

$$\hat{x} = x + Ut, \quad \hat{t} = t, \tag{50}$$

where $\hat{x}$ denotes horizontal distance from the origin of the travelling jet (figure 8*a*). The associated curvilinear coordinate $\hat{s}$ is such that

$$\frac{\mathrm{d}\hat{x}}{\mathrm{d}\hat{s}} = \frac{\mathrm{d}x}{\mathrm{d}s} = \cos\beta. \tag{51}$$

Using the chain rule, it follows that the time and spatial derivatives in balance equations (21)–(28) transform to

$$\frac{\partial\cdot}{\partial t} = \frac{\partial\cdot}{\partial\hat{t}} + \frac{U}{\cos\beta}\frac{\partial\cdot}{\partial\hat{s}}, \quad \frac{\partial\cdot}{\partial s} = \frac{\partial\cdot}{\partial\hat{s}}. \tag{52}$$

In the moving frame of reference, furthermore, the bed and ambient acquire apparent velocities $\hat{u}_0 = \hat{u}_\infty = U$, and the apparent velocity of the turbulent current becomes

$$\hat{v} = v + U/\cos\beta. \tag{53}$$

In terms of moving coordinates $(\hat{s}, \hat{t})$, transformed governing equations can be written

$$\frac{\partial z^{(0)}}{\partial\hat{t}} + \frac{U}{\cos\beta}\frac{\partial z^{(0)}}{\partial\hat{s}} = \sigma_0, \tag{54}$$

$$\frac{\partial h_1}{\partial\hat{t}} + \hat{v}\frac{\partial h_1}{\partial\hat{s}} + h_1\frac{\partial v}{\partial\hat{s}} = \sigma_1, \tag{55}$$

$$\frac{\partial h_2}{\partial\hat{t}} + \hat{v}\frac{\partial h_2}{\partial\hat{s}} + h_2\frac{\partial v}{\partial\hat{s}} = \sigma_2, \tag{56}$$

$$\frac{\partial \rho_1}{\partial\hat{t}} + \hat{v}\frac{\partial \rho_1}{\partial\hat{s}} = \sigma_\rho, \tag{57}$$

$$\frac{\partial k}{\partial\hat{t}} + \hat{v}\frac{\partial k}{\partial\hat{s}} = \sigma_k, \tag{58}$$

$$\frac{\partial v}{\partial \hat{t}} + \hat{v}\frac{\partial v}{\partial \hat{s}} + \frac{(\rho_1 - \rho_\infty)gh_1}{m}\frac{\partial h_1}{\partial \hat{s}} + \frac{\frac{1}{2}g\cos\beta\, h_1^2}{m}\frac{\partial \rho_1}{\partial \hat{s}} = \sigma_v, \tag{59}$$

where linear combinations were used to reduce (57) and (58) to standard advection-source equations, and where we have defined the source terms

$$\left.\begin{aligned} &\sigma_0 = -\frac{e^{(0)}}{\cos\beta}, \quad \sigma_1 = e^{(0)} - e^{(1)}, \quad \sigma_2 = e^{(1)} - e^{(2)}, \quad \sigma_\rho = \frac{\iota_1^{(0)} - \iota_1^{(1)}}{h_1}, \\ &\sigma_k = \{\tfrac{1}{2}(\tau_0^{(0)} + \tau_1^{(0)})v + \tfrac{1}{2}\tau_2^{(2)}(-v) - \tfrac{1}{2}g\cos\beta\, h_1(\iota_1^{(0)} + \iota_1^{(1)}) - k(i^{(0)} - i^{(2)}) - \gamma\}/m, \\ &\sigma_v = \{-\tau_1^{(0)} + \tau_2^{(2)} + (\rho_1 - \rho_\infty)h_1 g\sin\beta\}/m. \end{aligned}\right\} \tag{60}$$

Equations (54) to (59) represent six evolution equations for the six primitive variables $(z^{(0)}, h_1, h_2, \rho_1, k, v)$. Note that the primitive variables and source terms continue to include the original velocity v (without hat), which must now be interpreted as a current velocity relative to the stationary bed. In the convective derivatives $D/D\hat{t} = \partial/\partial\hat{t} + \hat{v}\partial/\partial\hat{s}$, on the other hand, it is the apparent velocity $\hat{v}$ (with hat) which intervenes. Although the six equations (54)–(59) constitute a complete set of governing equations, the balance equation for total sediment mass (26) will also be useful, and transforms to

$$\frac{\partial}{\partial \hat{t}}\{(\rho_0 - \rho_\infty)z^{(0)}\cos\beta + (\rho_1 - \rho_\infty)h_1\} + \frac{\partial}{\partial \hat{s}}\{(\rho_0 - \rho_\infty)z^{(0)}U + (\rho_1 - \rho_\infty)h_1\hat{v}\} = 0. \tag{61}$$

Its usefulness stems from the fact that it is the only equation that can be expressed in pure conservation form.

4.2. *Characteristic structure*

To analyse the system of quasi-linear equations (54)–(59), it is useful to first cast it in the matrix form

$$\frac{\partial \boldsymbol{V}}{\partial \hat{t}} + \boldsymbol{J}(\boldsymbol{V})\frac{\partial \boldsymbol{V}}{\partial \hat{s}} = \boldsymbol{S}(\boldsymbol{V}), \tag{62}$$

where

$$\boldsymbol{V} = \begin{pmatrix} z^{(0)} \\ h_1 \\ h_2 \\ \rho_1 \\ k \\ v \end{pmatrix}, \quad \boldsymbol{J} = \begin{pmatrix} \dfrac{U}{\cos\beta} & & & & & 0 \\ & \hat{v} & & & & h_1 \\ & & \hat{v} & & & h_2 \\ & & & \hat{v} & & 0 \\ & & & & \hat{v} & 0 \\ 0 & g_1 & 0 & \pi_1 & 0 & \hat{v} \end{pmatrix}, \quad \boldsymbol{S} = \begin{pmatrix} \sigma_0 \\ \sigma_1 \\ \sigma_2 \\ \sigma_\rho \\ \sigma_k \\ \sigma_v \end{pmatrix}, \tag{63}$$

and where we have introduced definitions

$$g_1 = \frac{(\rho_1 - \rho_\infty)\cos\beta\, h_1}{m}g, \quad \pi_1 = \frac{\frac{1}{2}g\cos\beta\, h_1^2}{m}. \tag{64}$$

Because only the diagonal and the last line and column of the Jacobian matrix $\boldsymbol{J}$ are non-zero, it is straightforward to derive its eigenstructure. Defining

$$c = \sqrt{g_1 h_1} = \sqrt{\frac{(\rho_1 - \rho_\infty)\cos\beta\, gh_1^2}{m}}, \tag{65}$$

the six eigenvalues of the matrix are

$$\lambda_0 = U/\cos\beta, \quad \lambda_\rho = \hat{v}, \quad \lambda_k = \hat{v}, \tag{66}$$

$$\lambda_* = \hat{v}, \quad \lambda_- = \hat{v} - c, \quad \lambda_+ = \hat{v} + c. \tag{67}$$

The first three eigenvalues λ_0, λ_ρ and λ_k are associated with (54), (57) and (58), which are already in characteristic form and are decoupled from the others. Eigenvalue λ_* is associated with advection of the depth ratio $h_1/(h_1+h_2)$ at the shared apparent velocity $\hat{v}$ of the two sublayers. Finally, λ_- and λ_+ are the speeds of the left and right internal gravity waves. Although there are at least three repeated eigenvalues, the system is endowed with a complete basis of six independent eigenvectors provided that $(\rho_1-\rho_\infty)h_1$ is non-zero (i.e. provided that suspended sand is present). The system is then hyperbolic. If the bottom current is entirely free of suspended sediment, on the other hand, eigenvalues λ_- and λ_+ and their eigenvectors collapse together, and the eigenvector basis becomes deficient.

As illustrated in figure 8, the jet-induced current will be assumed to flow from left to right, hence in what follows we restrict our attention to cases in which both $U>0$ and $\hat{v}>0$. Under these restrictions, the Jacobian matrix $\boldsymbol{J}$ will be regular everywhere except at locations where

$$\lambda_- = \hat{v} - c = 0, \tag{68}$$

causing the determinant to be equal to zero and the matrix to become singular. This will occur for the following critical value of the local Froude number

$$\hat{Fr} = \frac{\hat{v}}{c} = \frac{v + U/\cos\beta}{\sqrt{\{(\rho_1-\rho_\infty)\cos\beta\, g h_1^2\}/m}} = 1. \tag{69}$$

The above is a generalized definition of the internal Froude number, modified to account for the moving frame of reference, the sublayered structure, and the flow inclination. Using this revised definition, however, the Froude number can be interpreted as in standard hydraulics to precisely identify distinct regimes of flow. Where $\hat{Fr}>1$, the flow is supercritical, and all wave speeds of the system are oriented to the right, i.e. $\lambda_a>0$ for $a=0,\rho,k,*,-,+$. Where $\hat{Fr}=1$, the flow is critical, with a stationary wave speed $\lambda_-=0$, and a singular Jacobian matrix. Where $\hat{Fr}<1$, finally, the flow is subcritical, with five wave speeds oriented to the right, i.e. $\lambda_a>0$ for $a=0,\rho,k,*,+$ and one wave speed oriented to the left, $\lambda_-<0$.

4.3. *Longitudinal flow structure*

We now further restrict our attention to flows which have attained steady state in the moving frame of reference. The resulting solutions are known as travelling-wave solutions (see e.g. Hydon 2000). As discussed in § 1, such solutions are of great practical interest because dredging and jet trenching tools often operate continuously over great distances, allowing the flow pattern that they induce to converge to steady state in a frame of reference attached to the jetting device. Such solutions are obtained by setting the time derivatives $\partial/\partial\hat{t}$ to zero in (54)–(59). In matrix form, the reduced system of equation can be written

$$\boldsymbol{J}\frac{\mathrm{d}\boldsymbol{V}}{\mathrm{d}\hat{s}} = \boldsymbol{S}, \tag{70}$$

which represents a coupled system of 6 ordinary differential equations. Before integrating (70), we must first clarify the appropriate boundary conditions and consider the possible occurrence of critical sections where the matrix $\boldsymbol{J}$ will be singular.

For a horizontal sea bed, we anticipate that the jet-induced sediment motion will only take place over a finite distance behind the jetting device. Flowing to the right, the jet-induced current will dissipate energy until it is no longer able to sustain a sediment suspension. Consider the consequences of conservation equation (61), which

at steady state reduces to

$$\frac{\mathrm{d}}{\mathrm{d}\hat{s}}\{(\rho_0-\rho_\infty)z^{(0)}U+(\rho_1-\rho_\infty)h_1\hat{v}\}=0. \tag{71}$$

To the left, in front of the jetting device, the undisturbed sea bed has elevation $z^{(0)}=0$, and $(\rho_1-\rho_\infty)h_1=0$ (no sediment is yet in suspension). Integration of (71) therefore yields the invariant

$$(\rho_0-\rho_\infty)z^{(0)}U+(\rho_1-\rho_\infty)h_1\hat{v}=0. \tag{72}$$

Once jet-induced sediment transport occurs, therefore, $(\rho_1-\rho_\infty)h_1\hat{v}>0$ and the bed elevation will drop below the original sea bottom. Furthermore, it will remain below this level for as long as a suspended sediment flux is sustained. When this flux decreases, deposition will occur, and eventually the bed will recover its original elevation when all sediment motion has ceased. The temporary trench that is incised then backfilled in this fashion is precisely the objective of jet trenching, which seeks to bury the 'product' (cable or pipeline) under a protective layer of sediment after a single pass of the machine (see figure 1*c*).

Let us examine the conditions upstream and downstream of this travelling trench. Upstream, a high-speed clear-water jet impinges on the sand bed at location $\hat{x}=\hat{x}_I$. Since the jet has not yet eroded any sediment, $h_1(\hat{x}_I)=0$ and the shooting flow is clearly supercritical. In fact, the internal Froude number, (69), is infinite there, and the system of equations has not yet become hyperbolic. Less obviously, a similar situation holds at the downstream end of the trench. At a certain finite location $\hat{x}=\hat{x}_E$, the current has re-deposited its suspended sediment load, but retains a certain residual velocity $\hat{v}\neq 0$. Again, we therefore have a supercritical flow of infinite Froude number, where the equations cease to be hyperbolic.

The jet-induced current is therefore supercritical at both ends of the trench, and this leads to the question: Does the current stay supercritical throughout? In fact, we will show that this is indeed a possible outcome. There is, however, a second possible longitudinal flow structure, featuring two transcritical transitions: first, a discontinuous transition from super- to subcritical flow across an internal hydraulic jump (see figure 8*b*); then, a smooth passage back from sub- to supercritical across a critical section located at $\hat{x}=\hat{x}_C$ somewhere between the jump at $\hat{x}=\hat{x}_J$ and the trench end at $\hat{x}=\hat{x}_E$ (see figure 8*c*). The possible occurrence of two different travelling-wave structures (with or without shock) for flows induced by moving sources where the upstream conditions are supercritical was earlier identified by Hoffman (1967), in a problem of magnetogasdynamics (see also Whitham 1974). Steady profiles with and without hydraulic jumps have also been examined recently by Kostic & Parker (2007) for turbidity currents traversing a canyon/fan/canyon complex.

Regardless of the case, conditions at the upstream impingement point $\hat{x}=\hat{x}_I$ are supercritical, with six characteristics propagating from left to right, hence a need to prescribe boundary conditions there for all six primitive variables. We can then simply integrate system (70) from left to right, and proceed to the end of the trench if the flow is supercritical throughout. If the flow is transcritical, two additional difficulties must be addressed. First, means must be found to integrate through the discontinuous internal jump and through the singular critical section, assuming that their locations $\hat{x}_J$ and $\hat{x}_C$ are known. The more difficult issue, however, is that these locations are in fact unknown, and we must provide an additional internal boundary condition in order to close the problem. In the next section, we address these points one by one, starting with the specification of upstream boundary conditions.

5. Flow and solution details

5.1. *Jet expansion before impingement*

We examine first the development of the pure-water plane jet, before impingement onto the sand bed. A highly concentrated point-like source of momentum is considered, located at horizontal position $\hat{x} = 0$ and elevation Z above the unperturbed sea bed (figure 8*a*). This standoff elevation is taken to remain constant as the jetting device translates to the left. The jet is oriented at an angle α below the horizontal, where $0 < \alpha < 90°$. The jet-induced water speed is assumed to be much larger than the travelling speed, $v \gg U$, and the influence of the latter is neglected at this stage (i.e. we approximate $\hat{v} \approx v$). Before impingement, the problem considered is thus the expansion of a neutrally buoyant turbulent jet in a quiescent ambient. This is a classical problem of turbulence research, which need not be solved anew, but it is useful to treat it using the equations derived above in order to clarify their meaning and consequences. Measuring distance using curvilinear coordinate $\hat{s}$, defined again along the lower interface of the expanding jet, we can write equations

$$\frac{\mathrm{d}}{\mathrm{d}\hat{s}}(hv) = e^{(0)} - e^{(2)}, \tag{73}$$

$$\frac{\mathrm{d}}{\mathrm{d}\hat{s}}(\rho_2 h v^2) = 0, \tag{74}$$

$$\frac{\mathrm{d}}{\mathrm{d}\hat{s}}(\rho_2 h k v) = \tfrac{1}{2}\tau_2^{(0)} v + \tfrac{1}{2}\tau_2^{(2)}(-v) - \rho_2 h \varepsilon. \tag{75}$$

These three equations describe balance of volume, momentum and turbulence intensity, specialized to the case of a pure water jet in contact with a quiescent water ambient along both its upper and lower boundaries. They constitute reduced versions of (23), (28) and (44), with $h_1 = 0$ and $h = h_2$. The interface relations and semi-empirical functions described above can also be adapted to express

$$e^{(0)} = -e^{(2)} = \xi\sqrt{k}, \quad \tau_2^{(0)} = -\tau_2^{(2)} = \rho_\infty \xi \sqrt{k} v, \quad \varepsilon = \chi k^{3/2}/h. \tag{76}$$

Since $\rho_2 = \rho_\infty = \rho_W$ stays constant during the jet expansion, the equations reduce to

$$\frac{\mathrm{d}}{\mathrm{d}\hat{s}}(hv) = 2\xi\sqrt{k}, \tag{77}$$

$$\frac{\mathrm{d}}{\mathrm{d}\hat{s}}(hv^2) = 0, \tag{78}$$

$$\frac{\mathrm{d}}{\mathrm{d}\hat{s}}(hkv) = \xi\sqrt{k}v^2 - \chi k^{3/2}. \tag{79}$$

Using (78), we can express $h = \Sigma/v^2$ where $\Sigma = hv^2$ denotes the constant specific momentum flux of the jet. We now seek a similarity solution to (77)–(79) using the ansatz $\sqrt{k} = Av$, where A is a dimensionless constant to be determined. It can then be checked that the explicit solutions

$$h(\hat{s}) = 4\xi A \hat{s}, \quad v(\hat{s}) = \sqrt{\Sigma/h(\hat{s})}, \quad \sqrt{k(\hat{s})} = Av(\hat{s}), \tag{80}$$

satisfy (77)–(79) provided that constant A take the value $A = \sqrt{\xi/(\chi - 2\xi)}$. In accordance with a wealth of experimental data for plane turbulent jets, the result is a jet of linearly increasing thickness $h(\hat{s}) = 2\tan\delta\,\hat{s}$, where the wedge semi-angle δ is

such that

$$\tan\delta = 2\xi A = \sqrt{\frac{4\xi^3}{\chi - 2\xi}}. \tag{81}$$

Experiments further suggest for semi-angle δ values in the range $\delta = 6 - 8^\circ$ (Chen & Rodi 1980; Mathieu & Scott 2000; Durbin & Pettersson Reif 2001; Jirka 2006). In the present work, we choose for entrainment parameter ξ the value $\xi = 0.13$ which yields a semi-angle $\delta \approx 7^\circ$, in the middle of the above range.

Although similarity solutions strictly apply only beyond distances $\hat{s}$ of about 60 times the nozzle diameter (Panchapakesan & Lumley 1993), or about 3 cm for the present experiments, we also use the above water-jet solution to specify approximate boundary conditions upstream of the trench. At the bed impingement point $\hat{s} = \hat{s}_I = Z/\sin(\alpha + \delta)$, we set

$$z^{(0)} = h_1 = 0, \quad h_2 = 4\xi A \hat{s}_I, \quad \rho_1 = \rho_W, \quad v = \sqrt{\Sigma/h_2}, \quad k = A^2 v^2. \tag{82}$$

Jetting parameters which have an influence on the trenching process thus include the jet strength Σ, the standoff elevation Z and the jetting angle α. The above simplified jet geometry also places a further constraint on the erosion rate, associated with incipient detachment of the turbulent jet from the trenching front. If the erosion rate $e^{(0)}$ is high or the travelling speed U slow, unphysical bed profile angles β may be obtained in excess of the inclination $\alpha + \delta$ of the lower boundary of the free jet (see figure 8*a*). To ensure that the angle of the trenching front satisfies $\beta \leqslant \alpha + \delta$, the mass drift $\iota_1^{(0)}$ along the bottom will be subject to one further constraint:

$$\iota_1^{(0)} \leqslant (\rho_0 - \rho_1) U \sin(\alpha + \delta), \tag{83}$$

which will be enforced in addition to the constraint (49), whichever is more restrictive.

5.2. *Internal hydraulic jump*

Under conditions examined further below, it may be that the supercritical bottom current is not able to flow out of the scour hole it has itself incised without first undergoing an internal hydraulic jump (see figure 8*b*). In that case, the thin fast turbulent layer will make a sharp transition to a thick, slow current. There must be a corresponding conversion of the kinetic energy of the mean flow to potential energy, with an associated energy loss that may be transferred to some extent to the turbulent fluctuations. To describe this transition, assumed to occur as a sharp discontinuous jump at location $\hat{x} = \hat{x}_J$, shock relations must be derived. Conservation of volume, mass and momentum across the jump leads to equations

$$\left.\begin{array}{cc} [z^{(0)}U] = 0, & [h_1\hat{v}] = 0, \quad [h_2\hat{v}] = 0, \\ [\rho_1 h_1 \hat{v}] = 0, & [mv\hat{v} + \frac{1}{2}mc^2] = 0, \end{array}\right\} \tag{84}$$

where the square brackets denote a difference $[\eta] = \eta' - \eta$ between quantities sampled downstream (marked with a prime), and upstream of the jump (unmarked). In the shock relations (84), the apparent velocity $\hat{v} = v + U/\cos\beta$ is used as convective speed because we consider a jump that is stationary in the travelling frame of reference. It follows from (84) that the following quantities are preserved across the jump:

$$z'^{(0)} = z^{(0)}, \quad \frac{h_1'}{h'} = \frac{h_1}{h}, \quad \frac{h_2'}{h'} = \frac{h_2}{h}, \quad \rho_1' = \rho_1, \tag{85}$$

and the volume and mass fluxes $q = h\hat{v}$ and $\dot{m} = m\hat{v}$ are also shock invariants. The current thickness h' downstream of the jump is then given by the following relation

$$h' = \tfrac{1}{2}h\{\sqrt{1 + 8\hat{F}r^2} - 1\}. \tag{86}$$

This turns out to be identical to the classical jump relation of open-channel hydraulics (Bakhmeteff 1932), save for the non-standard definition (69) of the Froude number $\hat{F}r$.

An equation for the balance of mechanical energy can also be written

$$[\{\tfrac{1}{2}mv^2 + \tfrac{1}{2}(\rho_1 - \rho_\infty)g\cos\beta\, h_1^2 + mk\}\hat{v} + \tfrac{1}{2}(\rho_1 - \rho_\infty)g\cos\beta\, h_1^2 v] = -\Gamma, \tag{87}$$

where Γ is the rate of energy dissipation associated with the jump. Note in (87) that the convective flux component features apparent velocity $\hat{v}$, but the term associated with work of the pressure forces involves the original velocity v. Using relations (84)–(87), lengthy but straightforward algebra leads to the following relation

$$[mk\hat{v}] = \dot{m}\,[k] = \dot{m}c^2\frac{(h' - h)^3}{4h^2h'} - \Gamma, \tag{88}$$

governing the change in turbulence intensity $[k] = k' - k$ across the jump. The first term on the right-hand side of (88) is a production term associated with the mechanical energy lost by the mean flow, and constitutes a generalization of the dissipation formula for classical hydraulic jumps and bores (Stoker 1957). The second term on the right-hand side, Γ, denotes the rate of dissipation of the total mechanical energy (mean flow + turbulent fluctuations), by processes acting locally within the jump. We will neglect this term and simply set $\Gamma = 0$.

Whereas the flow thickness h on the upstream side of the jump is much smaller than both the trench depth H and its local radius of curvature $\mathfrak{R}$, this is not true on the downstream side of the jump, where $h \sim H \sim \mathfrak{R}$. As a result, the curvilinear description no longer applies, and we revert to a Cartesian view for the region $\hat{x} > \hat{x}_J$ downstream of the jump. In this region, we further apply the small-slope approximation

$$\sin\beta \approx \tan\beta, \quad \cos\beta \approx 1. \tag{89}$$

To ensure compatibility of the pressure thrust terms, which dominate on the downstream side of the jump, assumption (89) will be adopted for the shock relations as well. With this precision, (85), (86) and (88) provide a complete set of relations allowing us to compute the conjugate state downstream of the jump based on the known upstream state. The matter of determining the jump position $\hat{x}_J$, however, is left unresolved, and will be addressed in the next subsection together with the critical section.

5.3. *Passage through the critical section*

If the sediment-laden bottom current undergoes an internal hydraulic jump, then of necessity it must pass through a critical section before reaching the end of the trench. Let $\hat{x}_C$ be the location of this critical section, where the local Froude number takes the precise value $\hat{F}r = 1$ on the way back from sub- to supercritical flow. Where $\hat{F}r = 1$, however, the Jacobian matrix $\boldsymbol{J}$ is singular, and cannot be simply inverted to determine the primitive variable gradients $\mathrm{d}\boldsymbol{V}/\mathrm{d}\hat{s}$ at that location. In fact, the governing equations have no admissible solution at the critical section, unless the source vector $\boldsymbol{S}$ of system (70) satisfies there the solvability condition

$$\boldsymbol{S}^T\boldsymbol{W}^{(-)} = 0, \tag{90}$$

where superscript T denotes the transpose, and $\boldsymbol{W}^{(-)}$ is the left eigenvector of $\boldsymbol{J}$ associated with the zero eigenvalue λ_-. At the critical section, this eigenvector provides a basis for the left null space of the singular matrix. Condition (90) then states that admissible source vectors must be orthogonal to this left null space (see e.g. Strang 1988). The left eigenvector $\boldsymbol{W}^{(-)}$ is obtained from the condition

$$\boldsymbol{J}^T \boldsymbol{W}^{(-)} = \lambda_- \boldsymbol{W}^{(-)} = (\hat{v} - c)\boldsymbol{W}^{(-)}, \tag{91}$$

and is given by $\boldsymbol{W}^{(-)} = (0,\ g_1,\ 0,\ \pi_1,\ 0,\ -c)$. The solvability condition can then be written explicitly

$$\boldsymbol{S}^T \boldsymbol{W}^{(-)} = g_1\sigma_1 + \pi_1\sigma_\rho - c\sigma_v = 0, \tag{92}$$

where the products g_1, π_1 and source terms σ_a are given by (64) and (60). This is the missing internal boundary condition that we were looking for, and is all that is required in order to determine the positions $\hat{x}_J$ and $\hat{x}_C$ of the jump and critical section. An admissible jump location $\hat{x}_J$ will be such that the subcritical flow downstream of the jump satisfies solvability condition (92) at the precise location $\hat{x}_C$ where the Froude number reaches the value $\hat{F}r = 1$. The computational procedure used to determine locations $\hat{x}_J$ and $\hat{x}_C$ based on this criterion will be described in the next subsection.

To gain first a rough idea of what the distal end of the trench will look like, downstream of the jump, the following approximate solution is useful. We first neglect both the turbulent bottom shear stress and the turbulence intensity, i.e. we assume $\tau_1^{(0)} \approx 0$ and $k \approx 0$ for $\hat{x} > \hat{x}_J$. Equations (57), (54) and (58) then reduce to

$$\frac{\partial n_1}{\partial \hat{x}} = 0, \tag{93}$$

$$\frac{\partial z^{(0)}}{\partial \hat{x}} = \frac{n_1 \omega}{(n_0 - n_1)U}, \tag{94}$$

$$\hat{v}\frac{\partial v}{\partial \hat{x}} + \frac{(\rho_1 - \rho_\infty)g h_1}{m}\frac{\partial z^{(1)}}{\partial \hat{x}} = 0, \tag{95}$$

where the small-slope approximation (89) was invoked. Equations (93) and (94) show that the suspended sediment concentration remains constant, and that the bed profile takes a constant adverse slope controlled by the ratio of the settling rate ω to the travelling speed U. Assuming a small Froude number, we can furthermore neglect the first term on the left-hand side of the reduced equation of motion (95), and approximate

$$\frac{\partial z^{(1)}}{\partial \hat{x}} \approx 0. \tag{96}$$

As illustrated in figure 8(*c*), this approximate solution represents a turbid pool characterized by a nearly horizontal turbidity interface $z^{(1)} = z^{(0)} + h_1$, from which water is detrained and suspended sediment settles back to the bed. The depth h_1 of the turbid sublayer decreases approximately linearly with distance, until all suspended sediment has re-deposited and the trench ends. In the more complete description, the turbulence intensity will remain non-zero for some distance downstream of the jump, delaying this backfill process.

5.4. *Numerical solutions*

Although the above developments show that partial information can be obtained semi-analytically, solutions to the full governing equations must be sought numerically. Consider first the situation in which no jump is present. Integration of system (70) can then proceed from left to right, starting from the known conditions $\boldsymbol{V} = \boldsymbol{V}_I$ at the

impingement point. For this purpose, an explicit second-order Runge-Kutta scheme is used, advancing from curvilinear position $\hat{s}$ to position $\hat{s}+\Delta\hat{s}$ in the two successive sub-steps

$$\boldsymbol{V}(\hat{s}+\tfrac{1}{2}\Delta\hat{s}) = \boldsymbol{V}(\hat{s}) + \tfrac{1}{2}\Delta\hat{s}\,\boldsymbol{J}^{-1}(\boldsymbol{V}(\hat{s}))\,\boldsymbol{S}(\boldsymbol{V}(\hat{s})), \tag{97}$$

$$\boldsymbol{V}(\hat{s}+\Delta\hat{s}) = \boldsymbol{V}(\hat{s}) + \Delta\hat{s}\,\boldsymbol{J}^{-1}(\boldsymbol{V}(\hat{s}+\tfrac{1}{2}\Delta\hat{s}))\,\boldsymbol{S}(\boldsymbol{V}(\hat{s}+\tfrac{1}{2}\Delta\hat{s})). \tag{98}$$

In order to preserve exactly the invariant (72), however, the turbid sublayer density ρ_1 is adjusted after each sub-step using

$$\rho_1 = \rho_\infty + (\rho_0 - \rho_\infty)(-z^{(0)}U)/(h_1\hat{v}). \tag{99}$$

Integration halts when either one of the following conditions are met. If the depth h_1 of the turbid sublayer drops to zero, then the end of the trench has been reached, and the solution is complete. If, on the other hand, the Froude number decreases below critical value $\hat{F}r=1$ at some point along the way, then the assumption of a fully supercritical flow fails, and a solution featuring an internal hydraulic jump must be sought instead. Let us define function $F(\hat{x})$ as the value of the Froude number obtained at position $\hat{x}$ using supercritical integration. An admissible supercritical trench profile will then be such that $F_{min} = \min F(\hat{x}) > 1$.

To construct a solution with a jump, a supercritical integration is first performed as described above, starting from the point of impingement. Each point along the way is then a possible candidate for the location $\hat{x}_J$ of the internal hydraulic jump. We associate with each candidate jump position $\hat{x}_J$ a value of the solvability function $G(\hat{x}_J)$, constructed as follows. The jump relations (85)–(88) are used to determine the conjugate state $\boldsymbol{V}'(\hat{x}_J)$ immediately downstream of the assumed jump, based on the state $\boldsymbol{V}(\hat{x}_J)$ before the jump known from the supercritical integration. Integration of the subcritical profile is then continued, again from left to right, using the same Runge–Kutta scheme, until a section $\hat{x}_C$ is reached where the Froude number rises back to the critical value $\hat{F}r=1$. Having calculated the flow state $\boldsymbol{V}(\hat{x}_C)$ at that critical section, the local source terms $\boldsymbol{S}(\hat{x}_C)$ can be obtained from (60), hence the solvability product (92) can be evaluated at the critical section, i.e. $G(\hat{x}_J) = \boldsymbol{S}^T(\hat{x}_C)\boldsymbol{W}^{(-)}(\hat{x}_C)$. This is interpreted as a function of the jump position $\hat{x}_J$ since the profile downstream of the jump depends on where the jump is assumed to occur.

The equilibrated jump position sought is therefore such that $G(\hat{x}_J)=0$, and the problem becomes one of finding, if it exists, the root $\hat{x}_J$ of the solvability function G. This function takes negative values near impingement, rises in the downstream direction, then decreases again, taking a maximum $G_{max} = \max G(\hat{x}_J)$ at a certain candidate jump location $\hat{x}_{J,max} = \operatorname{argmax} G(\hat{x}_J)$. If $G_{max} > 0$, then a jump is possible in the interval $\hat{x}_I < \hat{x}_J < \hat{x}_{J,max}$. The function $G(\hat{x}_J)$ is found to be monotonous in this interval, hence it is straightforward to find the simple root $\hat{x}_J$ using bisection. Once this root has been found, we can continue the left-to-right integration past the critical section until the end of the trench is reached.

The conditions under which admissible solutions with and without jumps can be constructed can thus be summarized as follows. A fully supercritical profile (without jump) is such that $F_{min} > 1$. An admissible transcritical profile (with an internal jump along the way), on the other hand, is such that $G_{max} > 0$. Depending on the jet and sand properties, it turns out that three cases are possible. For certain values of the governing parameters, $F_{min} > 1$ and $G_{max} < 0$, implying that only the fully supercritical profile is admissible. For other values, $F_{min} < 1$ and $G_{max} > 0$, which means that only the solution with a jump is admissible. Finally, there is a domain of overlap where

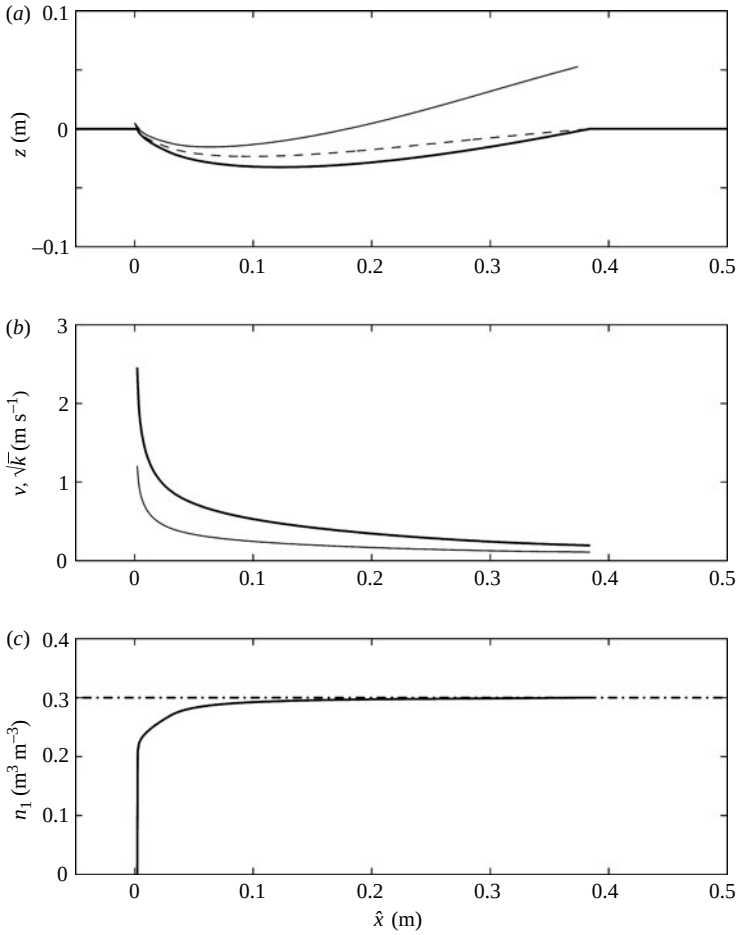

FIGURE 9. Computed travelling-wave solution for a fast speed of advance $U = 8\,\mathrm{cm\,s^{-1}}$: (*a*) bed interface $z^{(0)}$ (thick solid line), turbid interface $z^{(1)}$ (dashed line), and outer interface $z^{(2)}$ (thin solid line); (*b*) profiles of the current velocity v (thick solid line) and square root of the turbulence intensity $\sqrt{k}$ (thin solid line); (*c*) profile of the sand concentration n_1 in the turbid sublayer (thick solid line), with asymptotic value shown as dash-dotted line.

both $F_{min} > 1$ and $G_{max} > 0$, implying that both the solutions with and without jump are admissible. In that case, the travelling profiles adopted by the flow at steady state are not determined by the governing parameters alone, but depend on the full unsteady history of the flow.

Examples of computed profiles for these three cases are presented in figures 9, 10 and 11. For all cases, the model parameters are set to the values appropriate for the small-scale experiments described previously. Material parameters take values $\rho_S = 2670\,\mathrm{kg\,m^{-3}}$ (quartz sand), $\rho_w = 1000\,\mathrm{kg\,m^{-3}}$ (fresh water), sand concentration of the loose bed $n_0 = 0.6$, bed friction factor $f = 0.05$, and effective settling speed of the suspended sand $\omega = 3\,\mathrm{cm\,s^{-1}}$ (sand grains of median diameter $d_{50} = 0.33\,\mathrm{mm}$). The operating parameters of the jetting device are given the following values: jetting angle $\alpha = 60°$, standoff distance $Z = 0.5\,\mathrm{cm}$, jetting strength $\Sigma = 81\,\mathrm{s^{-2}}$. The only parameter that is varied between the three examples is the speed of advance U of the travelling jets.

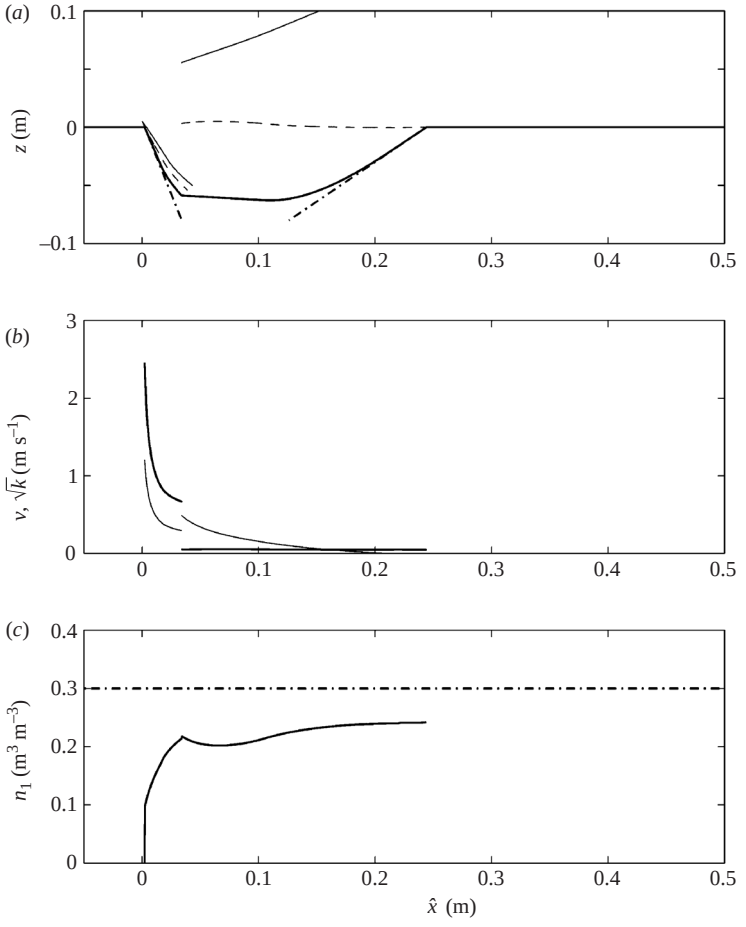

FIGURE 10. Computed travelling-wave solution for a slow speed of advance $U = 3\,\mathrm{cm\,s^{-1}}$: (*a*) bed interface $z^{(0)}$ (thick solid line), turbid interface $z^{(1)}$ (dashed line), and outer interface $z^{(2)}$ (thin solid line), with approximate solutions for the constrained trenching front and turbid pool re-sedimentation profile shown as a dash-dotted lines; (*b*) profiles of the current velocity v (thick solid line) and square root of the turbulence intensity $\sqrt{k}$ (thin solid line); (*c*) profile of the sand concentration n_1 in the turbid sublayer (thick solid line), with maximum value shown as dash-dotted line.

5.5. *Interpreted profiles*

Figure 9 shows computed steady profiles obtained for a relatively fast speed of advance $U = 8\,\mathrm{cm\,s^{-1}}$. For this speed, the only admissible solution features a supercritical profile throughout the trench. Figure 9(*a*) shows the computed profiles for interfaces $z^{(0)}$ (thick solid line), $z^{(1)}$ (dashed line), and $z^{(2)}$ (thin solid line). Bed interface $z^{(0)}$ exhibits a curved profile which transitions smoothly from a steep trenching front upstream to a backfill tail of milder adverse slope. In the upstream part of the trenching front, close to the point of impingement, the bed profile features a steep inclination that approaches, but does not attain, the maximum allowed inclination $\alpha + \delta = 67^\circ$. Comprised between the bed interface $z^{(0)}$ and the turbid interface $z^{(1)}$, the suspended sand layer thickens along the upstream portion, as a result of erosion and entrainment, before gradually thinning along the backfill tail where deposition and detrainment occur. The trench ends where the turbid layer reaches zero thickness,

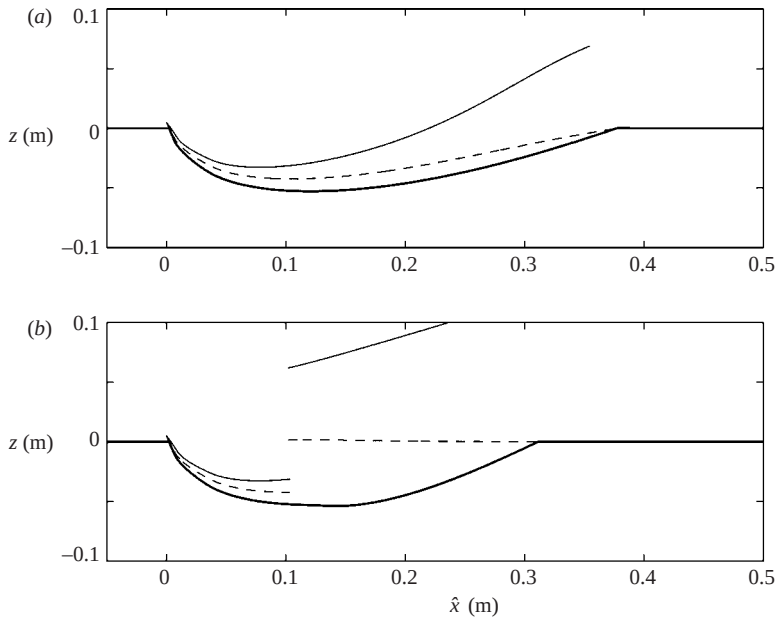

FIGURE 11. Computed travelling-wave solutions for intermediate speed of advance $U = 5\,\mathrm{cm\,s^{-1}}$: (*a*) shooting-flow solution (without jump); (*b*) alternative admissible solution featuring an internal hydraulic jump. The profiles shown are the bed interface $z^{(0)}$ (thick solid line), turbid interface $z^{(1)}$ (dashed line), and outer interface $z^{(2)}$ (thin solid line).

at which point the bed has returned to its original elevation. Throughout this erosional and depositional process, the turbulent bottom current, comprised between interfaces $z^{(0)}$ and $z^{(2)}$, monotonously increases in thickness as a result of the one-way entrainment of ambient water across the outer interface $z^{(2)}$. This freedom given to the turbid sublayer thickness to either grow or decay while the overall bottom current continuously thickens is a key feature of our proposed sublayered description.

Figures 9(*b*) and 9(*c*) show how the other variables evolve along the trench profile. The velocity v of the turbulent current and the square root $\sqrt{k}$ of its turbulence intensity are plotted in figure 9(*b*). As suggested by the simplified model of § 2.5, the velocity decreases roughly with the inverse of the square root of the along-bed distance, i.e. $v \propto 1/\sqrt{\hat{s}}$. This slowdown is the direct result of erosion and entrainment, which both induce mixing of the high-velocity turbulent current with initially motionless bed material and ambient water. Fast equilibration of production and dissipation of turbulent kinetic energy likewise lead to the scaling $\sqrt{k} \propto 1/\sqrt{\hat{s}}$, implying the approximate proportionality $\sqrt{k} \approx Cv$. Figure 9(*c*), finally, shows the evolution of the sediment concentration n_1 in the turbid sublayer. Starting from value $n_1 = 0$ at the point of impingement of the pure-water jet, this sand concentration rapidly converges towards an asymptotic maximum value $n_{1,max} = n_0/2$, shown as a dash-dotted line in the same figure. This can be understood as follows from the governing equations. Away from the trenching front, both constraints (49) and (83) eventually become inactive. At that point, the evolution equation for the density of suspended sediment in the turbid layer becomes

$$\frac{\mathrm{d}\rho_1}{\mathrm{d}\hat{s}} = \frac{\iota_1^{(0)} - \iota_1^{(1)}}{h_1 \hat{v}} = \frac{2\xi\sqrt{k}}{h_1 \hat{v}} \left\{ \tfrac{1}{2}(\rho_0 + \rho_\infty) - \rho_1 \right\}, \tag{100}$$

which takes the form of a non-equilibrium relation and implies that, asymptotically, the density of the turbid layer will tend towards a density $\rho_1 = (\rho_0 + \rho_\infty)/2$ intermediate between the densities of the underlying sediment bed and outer ambient. For the suspended sediment concentration n_1, the asymptotic result is $n_1 \to n_0/2$. Because of the upstream boundary conditions, constraints (49) and (83), and the lag distance required for equilibration, however, the concentration will start from below and never quite reach this value. Value $n_{1,max} = n_0/2$ thus constitutes an upper bound for the suspended sediment concentration that can be attained in the turbid sublayer.

Figure 10 shows corresponding plots for a slower speed of advance, set to value $U = 3\,\mathrm{cm\,s^{-1}}$, with all other parameters kept the same as before. For this case, the only admissible solution features an internal hydraulic jump. As illustrated in figure 10(*a*), the eroding jet first plunges down a steep trenching front, limited by constraint (83) shown as a dash-dotted line. This intense erosion is cut short when the thin shooting current undergoes an internal hydraulic jump, beyond which the turbid interface slightly overshoots the original sea-bed level. Shown in figure 10(*b*), the current velocity v undergoes a sudden drop at the jump transition. The modelled turbulence intensity k, on the other hand, rises across the jump owing to the assumed energy transfer from the mean flow. This enhanced turbulence intensity allows the slower flow to erode the sea-bed gently beyond the jump, delaying re-deposition until further downstream.

Eventually, turbulence dissipates, at which point the backfill limb of the trench approaches the turbid pool approximation of (93)–(96), with a linear rise of the bed profile (dash-dotted line), back to the undisturbed sea-bed level where the trench terminates. For this case, the jump is located at position $\hat{x}_J = 0.034$ m, such that the steady flow passes smoothly through a critical section at position $\hat{x}_C = 0.221$ m, before the trench ends at position $\hat{x}_E = 0.244$ m. Figure 10(*c*) shows how the sand concentration in the turbid sublayer rises along the supercritical upstream stretch of the profile, then drops slightly immediately after the jump, where entrainment of ambient water exceeds erosion of bed material. The suspended sand concentration then rises again to approach a constant value in the downstream turbid-pool region, but this value lies below the limiting concentration $n_{1,max} = n_0/2$ (dash-dotted line).

Figure 11 shows the case of intermediate speed of advance, set here to value $U = 5\,\mathrm{cm\,s^{-1}}$, with all the other parameters again left unchanged. For this speed, the admissibility conditions overlap, and solutions with and without a jump can both be constructed. Figure 11(*a*) shows the flow pattern computed under the assumption that no jump forms, while figure 11(*b*) shows the resulting profiles when a jump is introduced. Both flows represent admissible steady-state solutions for the exact same model and operating parameters. The resulting profiles are therefore strictly identical in their upstream portion, where the flow is supercritical. Figure 11(*a*) shows how the supercritical profiles can be continued to the end of the trench without any regime transition. The current gradually expands, but remains thin throughout the erosion and deposition process. Figure 11(*b*), on the other hand, shows the alternative steady profiles obtained when an internal jump is allowed to form. The flow then undergoes a sudden expansion at the jump, with the turbid sublayer invading the whole depth of the trench. Eventually, however, the suspended sand settles back to the bed which rises back to its original level. Owing to the local turbulence enhancement associated with the jump, scour in figure 11(*b*) reaches slightly deeper than in figure 11(*a*), but the resulting trench length is shorter.

In the literature, the possible coexistence of two possible steady states, with and without jump, is known to occur for other types of shallow flow. This includes the

case of single-layer flow over a moving obstacle described by Baines (1995). We find here that the same situation occurs for erosional bottom currents induced by moving plane jets. To summarize, the present shallow-flow theory predicts that the jet-induced flow will take the form of a shooting current for high enough speeds of advance. As this speed is decreased, the jet will incise a deeper trench, inside which the flow may or may not undergo an internal jump. If the speed is decreased further, the sediment-laden flow becomes forced to go through a jump. These general predictions of the theory, as well as the more specific features of the computed profiles, must now be checked against the laboratory observations.

6. Comparison of theory and experiments

6.1. *Longitudinal profiles*

To permit qualitative and quantitative evaluations of the theory, figures 12 and 13 show computed and observed profiles for low and high values of the jetting strength Σ, respectively. For each jetting strength, results for four different speeds of advance U are shown, and ordered from fast to slow speeds in (a) to (d) for each figure. In accordance with the theoretical calculations, both series feature purely shooting flows for high speeds of advance (figures 12a, b and 13a), but exhibit internal hydraulic jumps for slower speeds (figures 12c, d and 13b–d).

For the purely shooting flows of figure 12(a, b), the bed profile adopts a characteristic 'swoosh'-shaped curve, similar to the profile of figure 6(c) calculated using the simplified theory of § 2.5. The corresponding asymmetric profile smoothly blends together a steep trenching front with a gentle backfill tail. In the presence of a strong hydraulic jump, by contrast (figure 12c, d), the bed profile features three distinct zones: a steep erosional trenching front, a nearly horizontal zone of delayed deposition, then a linearly rising backfill limb. These observed features are seen to be reproduced well by the computations. Whereas the bed profile measurements (filled circles) are unambiguous and can be identified with the predicted bed interface profile $z^{(0)}$ (thick solid line), the observed outer limit of suspended sand (open circles) is more diffuse, and can only be expected to lie somewhere between turbid interface $z^{(1)}$ (dashed line) and the outer turbulent current boundary $z^{(2)}$ (thin solid line), both modelled as sharp discontinuities. The corresponding distributions of flow velocity and sediment concentration along normal-to-bed transects are modelled as step functions, whereas the actual distributions are gradually varied. Moreover, the internal hydraulic jump is modelled by the theory as a localized shock, whereas, in practice, the jump develops over a certain length. Despite these limitations, the flow-thickness evolution depicted by the calculations and by the experimental profiles exhibit similar trends. For the shooting-flow runs, the sediment-laden current remains comparatively thin as it flows along the streamlined profile of the incised trench. In the presence of an internal jump, on the other hand, the current suddenly thickens before re-depositing its suspended sediment.

Figure 13 shows the influence of an increased jetting strength, leading to deeper and longer trenches. The flow goes from a shooting regime (figure 13a) to a strong internal jump (figure 13d), with intermediate stages (figure 13b, c) featuring a weaker internal jump. Although agreement is poorer for these intermediate stages, the overall trend from absent to weak to strong jump as the trench is scoured deeper is captured well by the computed profiles. While limited in its accuracy for any given individual run, the level of agreement obtained in figures 12 and 13 is nevertheless

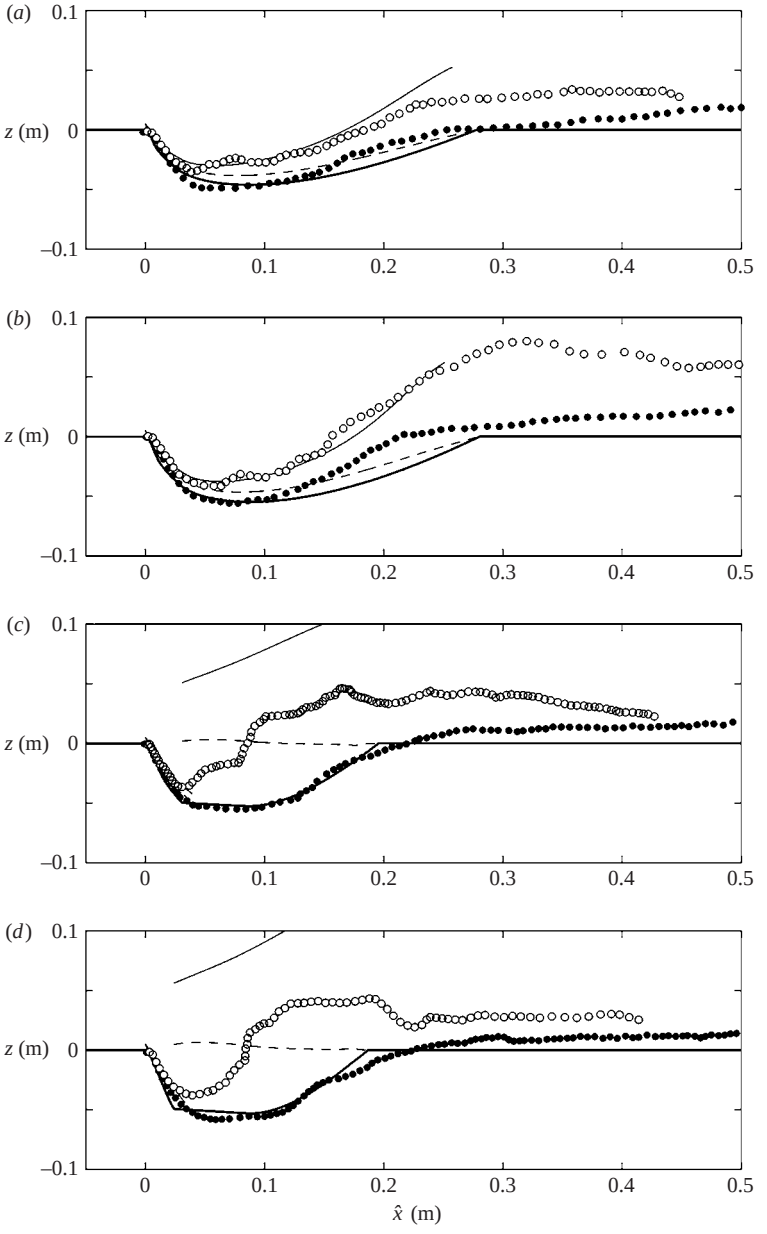

FIGURE 12. Comparison of observed and computed profiles for low jetting strength $\Sigma = 5.81\,\mathrm{s}^{-2}$ at various speeds of advance: (*a*) $U = 4.0\,\mathrm{cm\,s}^{-1}$; (*b*) $U = 3.5\,\mathrm{cm\,s}^{-1}$; (*c*) $U = 2.9\,\mathrm{cm\,s}^{-1}$; (*d*) $U = 2.4\,\mathrm{cm\,s}^{-1}$. Filled circles = measured bed profile; open circles = measured outer limit of suspended sediment; curves = computed profiles for the bed interface $z^{(0)}$ (thick solid line), turbid interface $z^{(1)}$ (dashed line), and outer interface $z^{(2)}$ (thin solid line).

significant because all computations are performed under the same values of the model parameters.

Among these parameters, tuning was required only for the friction factor f (set to value $f = 0.05$), and for the effective settling speed (set to value $\omega = 3\,\mathrm{cm\,s}^{-1}$), all other constitutive constants being obtained from either generic experiments (e.g. plane

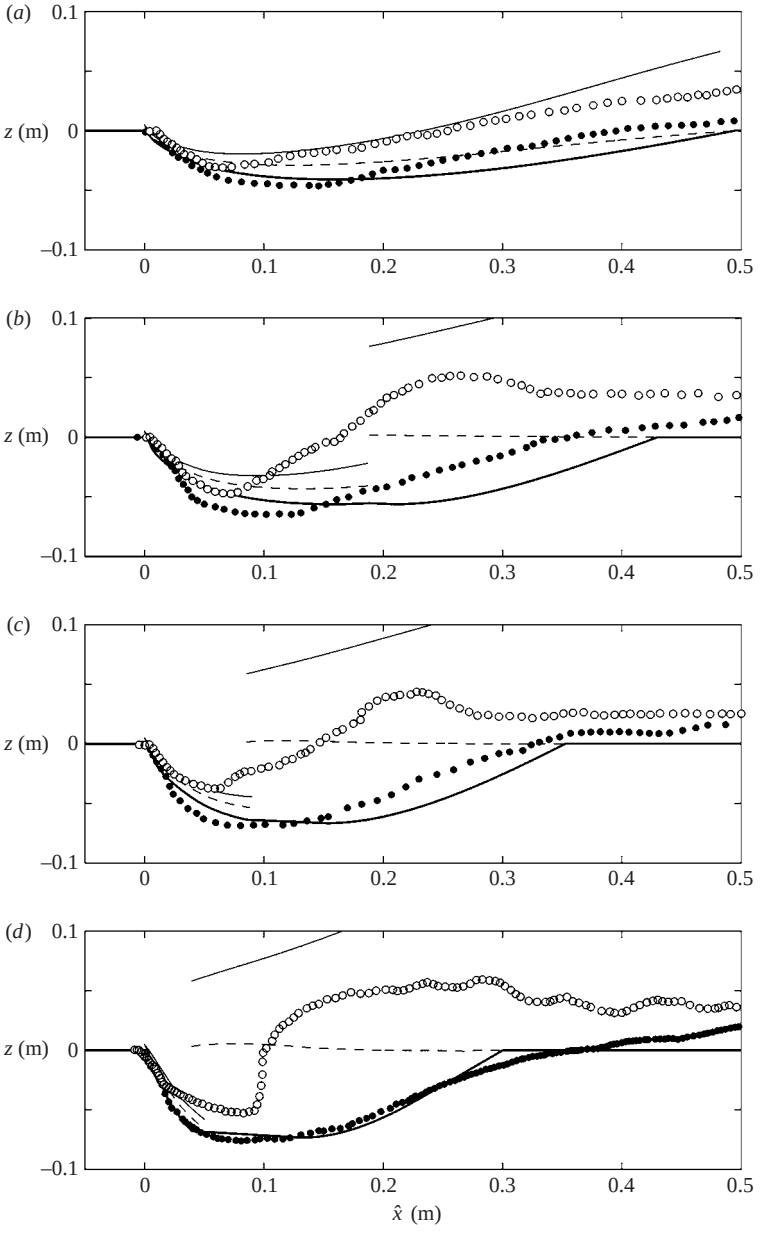

FIGURE 13. Comparison of observed and computed profiles for high jetting strength $\Sigma = 10.61\,\mathrm{s}^{-2}$ at various speeds of advance: (*a*) $U = 8.6\,\mathrm{cm\,s}^{-1}$; (*b*) $U = 6.3\,\mathrm{cm\,s}^{-1}$; (*c*) $U = 5.0\,\mathrm{cm\,s}^{-1}$; (*d*) $U = 3.2\,\mathrm{cm\,s}^{-1}$. See the caption to figure 12 for symbol definitions.

jet spreading rates) or standard material tests. A higher friction factor f increases erosion and leads to deeper and longer trenches, without greatly affecting the aspect ratio H/L, where H and L are, respectively, the trench depth and trench length. The effective settling speed ω, on the other hand, influences both the size and aspect ratio of the trench, with larger sizes and smaller H/L ratios obtained for lower values of the effective settling speed. Although results are sensitive to the precise choice of f and ω, the tuned values nevertheless fall within the range expected from past work

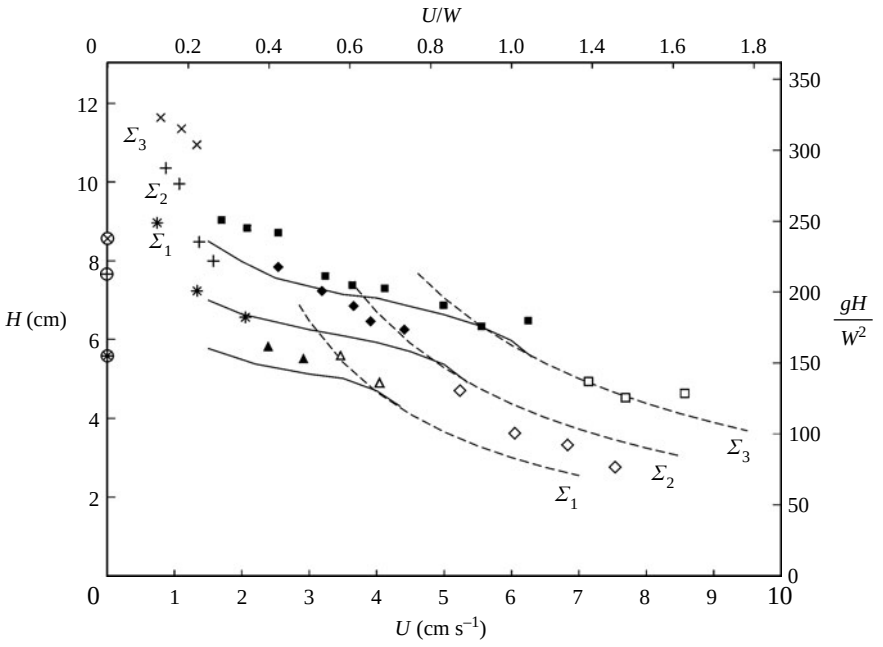

FIGURE 14. Relation between trench depth H and speed of advance U: symbols = experimental observations for different jetting strengths $\Sigma_1 = 5.81\,\mathrm{s}^{-2}$ (*, △), $\Sigma_2 = 8.11\,\mathrm{s}^{-2}$ (+, ◇) and $\Sigma_3 = 10.61\,\mathrm{s}^{-2}$ (×, □); curves = computed relations $H(U)$ parameterized by the jetting strength Σ for values Σ_1, Σ_2, Σ_3; circled symbols = stationary jets; algebraic symbols = separated flows; filled symbols and solid lines = flows with internal jump; open symbols and dashed lines = shooting flows.

(for the friction factor) and from our settling column tests (for the settling speed). Without forcing or case-by-case tuning, the proposed model is thus able to predict the main features of the system response over a range of jetting conditions.

6.2. *Trench depth*

Figure 14 further documents the dependence of the trench depth H on the speed of advance U and jetting strength Σ, using data from a larger set of 38 experimental runs. The trench depth is defined as the maximum drop of the bed profile below its initial level, i.e. $H = \max(-z^{(0)}(\hat{x}))$. As noted previously, this depth tends to increase for higher jetting strengths and slower speeds of advance. In figure 14, data points from runs with and without a hydraulic jump are plotted using filled and open symbols, respectively, with different symbol shapes associated with the three jetting strengths tested $\Sigma_1 = 5.81\,\mathrm{s}^{-2}$, $\Sigma_2 = 8.11\,\mathrm{s}^{-2}$, and $\Sigma_3 = 10.61\,\mathrm{s}^{-2}$. For comparison, calculated curves for the internal jump case and purely shooting-flow case are plotted as solid and dashed lines, respectively. For intermediate speeds of advance, both types of solution are admissible and the two sets of curves overlap.

For jetting strengths Σ_1 and Σ_3, the obtained relationship between trench depth and speed of advance features a break of trend at the transition between regimes with and without jumps. In the absence of internal jump, the trench depth varies roughly with the inverse of the speed of advance (dashed lines and open symbols). A deeper trench results when the sand bed is exposed longer to the erosive action of the jet. Although the trench depth continues to increase for the slower speeds of advance at which an internal hydraulic jump forms (solid lines and filled symbols),

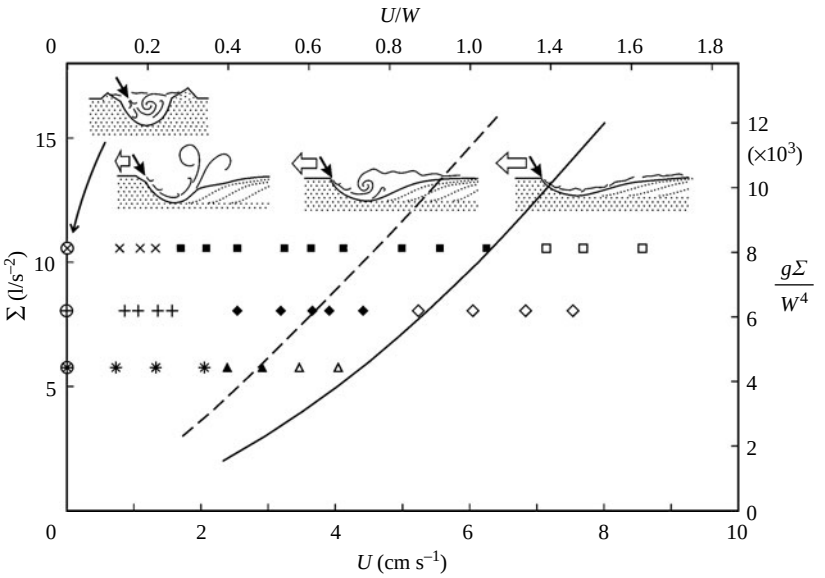

FIGURE 15. Phase diagram showing the parametric domains of the different flow patterns (cartoons), depending on jetting strength Σ and speed of advance U. Symbols denote experimental observations, using the same code as figure 14. The curves represent the theoretical boundaries of the shooting-flow and jump regimes: the solid line is the locus $G_{max} = 0$ representing the maximum speed of advance at which a jump can form; the dashed line is the locus $F_{min} = 1$ representing the minimum speed of advance of purely shooting flows. The sector between the two curves is the domain of overlap in which both solutions (with and without jump) are admissible.

the corresponding depths are lower than would be expected from extrapolating to the left the inverse relation observed for the shooting flows. This indicates that the internal jump tends to curtail the trench depth that would otherwise be reached in its absence. Overall, the observed and computed depths are in reasonable agreement with each other over the range of jetting strengths and speeds of advance for which the theory applies.

For completeness, we have also included in figure 14 the trench depth measurements obtained for very slow speeds of advance (see figure 5*b*), in which the flow separates and fountains upwards, and for stationary jets (see figure 5*a*). The strongly deflected jet obtained at very slow speeds of advance (algebraic symbols) generates the deepest trenches. For stationary jets, on the other hand (circled algebraic symbols), the formation of lateral levees and roll-up of the flow into a recirculating vortex lead to smaller trench depths, in line with results for flows with internal jump. Qualitatively, we may thus interpret the stationary case as a type of drowned internal hydraulic jump. As discussed earlier, the more complicated flow patterns obtained for the very slow and stationary cases render our theory inapplicable.

6.3. *Phase diagram*

To summarize the above findings, computations and observations of the domain of occurrence of various flow regimes are represented in figure 15 as a phase diagram. The two governing parameters examined are the speed of advance U and jetting strength Σ, with other parameters kept constant. Going from left to right in the diagram, the experimentally observed flows are classified into four groups: stationary jetting flows

(circled algebraic symbols), obtained when the jetting head is held fixed; separated flows (algebraic symbols), observed at very slow speeds of advance; flows with an internal hydraulic jump (filled symbols) observed at slow speeds; and shooting flows (open symbols) observed at high speeds of advance. These correspond, respectively, to figures 5(*a*) to 5(*d*), reproduced in cartoon form on the phase diagram of figure 15. To facilitate comparison with results from other tests, we have provided in figures 14 and 15 alternative abscissae and ordinates expressed in dimensionless form, taking the fall speed W and acceleration due to gravity g as normalizing variables.

On the same diagram, lines are used to delineate the domains of admissibility of solutions with and without jump, as computed on the basis of our shallow-flow theory. The solid line denotes condition $G_{max} = 0$ which, for a given jetting strength, represents the fastest speed of advance at which a jump may form. The dashed line denotes condition $F_{min} = 1$, which likewise represents the slowest speed of advance at which the flow can remain supercritical throughout the trench. The sector comprised between these two curves represents the domain of overlap in which both types of solution are admissible.

Agreement between theory and experiments requires that only open symbols (shooting flows) be observed to the right of the solid line, and that only solid symbols (flows with internal jumps) be found to the left of the dashed line, with both types of symbol allowed inside the sector of overlap (where both flow patterns can theoretically occur). The observations are found to be consistent with these domain predictions. Nevertheless, we emphasize again that the experiments conducted at zero and very slow speeds of advance (circled and uncircled algebraic symbols) lie outside the scope of the theory. For these conditions, the jet-induced flow either rolls up into a spanwise vortex or separates from the bed, and the theory breaks down.

7. Conclusions

In the present work, theory and experiments were used to examine underwater sand beds exposed to the geomorphic action of travelling plane jets. This jetting action leads to the formation of a translating scour hole of permanent shape, in which the turbulent current negotiates a dynamic equilibrium with the curved bed profile. The turbulent underflow erodes and deposits sediment from the static bed, while simultaneously entraining quiescent water from the outer ambient. Because of sediment suspension, the bottom current acquires a higher density than the ambient, allowing gravity to affect both the turbulence generation and the longitudinal balance of the flow. In particular, gravitational influence on the sediment-laden current can be strong enough to force a transition between supercritical and subcritical flow, leading to the formation of an internal hydraulic jump.

As a result, the jet-induced bottom currents can equilibrate into two types of steady profiles inside the travelling trench: shooting flows, which remain thin throughout, or flows featuring a sudden expansion at the internal hydraulic jump. For constant jetting strength, the transition from shooting-flow to internal-jump regimes takes place when the speed of advance of the travelling jet goes from fast to slow. Slower speeds of advance lead to longer exposure of the bed to the erosional action of the plane jet, leading to a deeper scour hole. Eventually, the sediment-laden current cannot flow out of the deep hole it has dug itself into without first undergoing an internal jump. By slowing down the current, the jump curtails its erosive action and acts as a limiter on the trench depth. Internal-jump formation also leads to trenches of shorter length. On the downstream side of the jump, the sediment-laden current ponds into a turbid pool where sand grains settle back to the bed.

To elucidate these processes, shallow-flow theory was found to provide a valuable tool. Viewing the jet-induced flow as a sublayered current delimited by sharp interfaces across which transfers of mass and momentum occur provides a simple, but versatile framework in which erosion and entrainment effects can be modelled together. By complementing mass and momentum balance with an energy budget, furthermore, the dynamics of stratified turbulence can be taken into account. The treatment can be extended further to steep, but gradually curved profiles, by using curvilinear coordinates. Provided shallow-flow theory is extended in this fashion, the key notions of classical hydraulics become applicable to the jet trenching problem. This includes a precise identification of supercritical and subcritical regimes, along with their transitions through hydraulic jumps and control sections. Most importantly, the resulting predictions turn out to be in reasonably good agreement with laboratory experiments. Shooting flows and internal jump flow patterns are observed, and their profiles and range of occurrence accord with the shallow-flow computations.

Nevertheless, the present results are subject to a number of restrictive limitations. First, experimental test of the theory was limited to a narrow range of conditions, featuring a single jetting geometry and only one sand size. We expect the range of observable behaviour to expand significantly if more varied conditions are examined, stretching the ability of the theory to keep up. Secondly, even for the limited range of conditions examined in the present experiments, some significant flow features clearly fall outside the scope of the proposed theory. For plane jets travelling very slowly along the bed, gravity-induced breaching occurs ahead of jet impingement, whereas further into the trench the jet-induced current undergoes a strong deflection away from the bed. The recirculating roller obtained for stationary jets likewise renders our theory inapplicable. Paradoxically, jets translating at sufficient speed thus appear more amenable to theoretical treatment than the more basic case of stationary jets.

Finally, the configuration examined in the present paper is far simpler that the conditions of interest in actual trenching and dredging operations. Challenges encountered in practice include three-dimensional water and sediment motions, more complex soil responses affected by cohesion, sorting and liquefaction, and seafloors featuring varied bathymetry such as slopes, sand waves and pre-existing cables and pipelines. For some of these challenges, further scientific study may yield useful results in support of technical ingenuity.

Financial support for the present work was provided by the Taiwan National Science Council under grant 94-2211-E002-040. J.-F. Vanden Berghe, of Fugro Engineers NV/SA in Brussels, Belgium, provided the initial impetus for our study, as well as continued feedback and support. Peter H. T. Liu and F. L. Lian helped set up the moving jet experiments, and the stationary jet tests were performed by Jason C. C. Su and Y. H. Wu. Additional guidance and feed-back from D. Cathie, H. T. Chou, C. K. Lin, T. S. Ueng and D. L. Young and the anonymous reviewers are also gratefully appreciated. We wish to dedicate this paper to the memory of Professor Howell Peregrine, Associate Editor of the *Journal of Fluid Mechanics*, who handled the initial submission of the manuscript before his death on 20 March 2007.

REFERENCES

Abbott, M. B. 1979 *Computational Hydraulics. Elements of the Theory of Free Surface Flows*. Pitman.

Aderibigbe, O. O. & Rajaratnam, N. 1996 Erosion of loose beds by submerged circular impinging vertical turbulent jets. *J. Hydraul. Res.* **34**, 19–33.

Bagnold, R. A. 1966 An approach to the sediment transport problem from general physics. *US Geol. Surv. Prof. Paper* 422-I.

Baines, P. G. 1995 *Topographic Effects in Stratified Flows*. Cambridge University Press.

Bakhmeteff, B. A. 1932 *Hydraulics of Open Channels*. McGraw-Hill.

Bombardelli, F. A. & Gioia, G. 2006 Scouring of granular beds by jet-driven axisymmetric turbulent cauldrons. *Phys. Fluids* **18**, art. 088101, 1–4.

Chen, C. J. & Rodi, W. 1980 *Vertical Buoyant Jets: A Review of Experimental Data*. Pergamon.

Chen, H., Crosta, G. B. & Lee, C. F. 2006 Erosional effects on runout of fast landslides, debris flows and avalanches: a numerical investigation. *Géotechnique* **56**(5), 305–322.

Crowe, C. T. 2000 On models for turbulence modulation in fluid–particle flows. *Intl J. Multiphase Flow* **26**, 719–727.

Dronkers, J. 2005 *Dynamics of Coastal Systems*. World Scientific.

Durbin, P. A. & Pettersson Reif, B. A. 2001 *Statistical Theory and Modeling for Turbulent Flows*. Wiley.

Ellison, T. H. & Turner, J. S. 1959 Turbulent entrainment in stratified flows. *J. Fluid Mech.* **6**, 423–448.

Fraccarollo, L. & Capart, H. 2002 Riemann wave description of erosional dam-break flows. *J. Fluid Mech.* **461**, 183–228.

Fredsøe, J. & Deigaard, R. 1992 *Mechanics of Coastal Sediment Transport*. World Scientific.

Gioia, G. & Bombardelli, F. A. 2005 Localized turbulent flows on scouring granular beds. *Phys. Rev. Lett*. **95**, art. 014501, 1–4.

Guy, H. P., Simons, D. B., & Richardson, E. V. 1966 Summary of alluvial channel data from flume experiments, 1956–1961, *Geol. Surv. Prof. Paper* 462-I.

Hoffman, A. L. 1967 A single fluid model for shock formation in MHD shock tubes. *J. Plasma Phys*. **1**, 193–207.

Hogg A. J., Huppert, H. E. & Dade, W. B. 1997 Erosion by planar turbulent wall jets. *J. Fluid Mech*. **338**, 317–340.

Hopfinger, E. J., Kurniawan, A., Graf, W. H. & Lemmin, U. 2004 Sediment erosion by Görtler vortices: the scour-hole problem. *J. Fluid Mech*. **520**, 327–342.

Hsu, T.-J., Jenkins, J. T. & Liu, P. L.-F. 2003 On two-phase sediment transport: dilute flow. *J. Geophys. Res*. **108**(C3), art. 3057, 1–14.

Hydon, P. E. 2000 *Symmetry Methods for Differential Equations*. Cambridge University Press.

Jirka, G. H. 2006 Integral model for turbulent buoyant jets in unbounded stratified flows. Part 2: Plane jet dynamics resulting from multiport diffuser jets. *Environ. Fluid Mech*. **6**(1), 43–100.

Knox, D., Krumholz, D. J. & Clausner, J. E. 1994 Water injection dredging in the United States. In *Proc. Second Intl Conf. on Dredging and Dredged Material Placement* (ed. E. Clark McNair, Jr), pp. 847–856, ASCE.

Kobayashi, N. & Johnson, B. D. 2001 Sand suspension, storage, advection, and settling in surf and swash zones. *J. Geophys. Res*. **106**(C5), 9363–9376.

Kobayashi, N. & Tega, Y. 2002 Sand suspension and transport on equilibrium beach. *ASCE J. Waterways, Port, Coastal, Ocean Engng* **128**(6), 239–248.

Kolmogorov, A. N. 1941 The local structure of turbulence in incompressible viscous fluid for very large Reynolds number. *Dokl. Akad. Nauk SSSR* **30**, 301–305. [English translation *Proc. R. Soc. Lond*. A (1991) **434**, 9–13.]

Kostic, S. & Parker, G. 2007 Conditions under which a supercritical turbidity current traverses an abrupt transition to vanishing bed slope without a hydraulic jump. *J. Fluid Mech*. **586**, 119–145.

Machin, J. 2001 *Recent Research on Cable Jet Burial*. Perry Slingsby Systems, Jupiter, Florida.

Mastbergen, D. R. & Van den Berg, J. H. 2003 Breaching in fine sands and the generation of sustained turbidity currents in submarine canyons. *Sedimentology* **50**, 625–637.

Mathieu, J. & Scott, J. 2000 *An Introduction to Turbulent Flow*. Cambridge University Press.

Mazurek, K. A., Rajaratnam, N. & Sego, D. C. 2003 Scour of a cohesive soil by submerged plane turbulent wall jets. *J. Hydraul. Res*. **41**(2), 195–206.

van Melkebeek, E. 2002 Pre-trenching, pre-sweeping and backfilling for the 36" offshore pipeline project in Taiwan. *Terra Aqua* **87**(3), 19–25.

Mohamed, M. S. & McCorquodale, J. A. 1992 Short-term local scour. *J. Hydraul. Res.* **30**(5), 685–699.

Panchapakesan, N. R. & Lumley, J. L. 1993 Turbulence measurements in axisymmetric jets of air and helium. Part 1. Air jet. *J. Fluid Mech.* **246**, 197–223.

Parker, G., Fukushima, Y. & Pantin, H. M. 1986 Self-accelerating turbidity currents. *J. Fluid Mech.* **171**, 145–181.

Perng, A. T. H. 2006 Trenching of underwater sand beds by steadily moving jets. PhD thesis, Graduate Institute of Civil Engineering, National Taiwan University.

Rajaratnam, N. 1981 Erosion by plane turbulent jets. *J. Hydraul. Res.* **19**, 339–358.

Raubenheimer, B., Elgar, S. & Guza, R. T. 2004 Observations of swash zone velocities: a note on friction coefficients. *J. Geophys. Res.* **109**(C1), C01027, 1–8.

Richardson, J. F. & Zaki W. N. 1954 Sedimentation and fluidisation, Part 1. *Trans. Instn Chem. Engrs* **32**, 35–53.

van Rijn, L. C. 1984 Sediment transport, part II: suspended load transport. *J. Hydraul. Engng ASCE* **110**(11), 1613–1641.

Rouse, H. 1937 Modern conceptions of the mechanics of fluid turbulence. *Trans. ASCE* **102**, 532–536.

Rouse, H. 1940 Criteria for similarity in the transportation of sediment. *Proc. Hydraul. Conf., Univ. of Iowa Studies in Engineering*, Bulletin 20, pp. 32–49.

Stein, O. R., Julien, P. Y. & Alonso, C. V. 1993 Mechanics of jet scour downstream of a headcut. *J. Hydraul. Res.* **31**, 723–738.

Stoker, J. J. 1957 *Water waves*. Interscience.

Strang, G. 1988 *Linear Algebra and its Applications*. Brooks/Cole.

Sumer, B. M., Kozakiewicz, A., Fredsøe, J. & Deigaard, R. 1996 Velocity and concentration profiles in sheet-flow layer of movable bed. *J. Hydraul. Engng ASCE* **122**, 549–558.

Ten Cate, A., Derksen, J. J., Portela, L. M. & Van den Akker, H. E. A. 2004 Fully resolved simulations of colliding monodisperse spheres in forced isotropic turbulence. *J. Fluid Mech.* **519**, 233–271.

Ungarish, M. 1993 *Hydrodynamics of Suspensions*. Springer.

Van den Berg, J. H., Van Gelder, A. & Mastbergen, D. R. 2002 The importance of breaching as a mechanism of subaqueous slope failure in fine sand. *Sedimentology* **49**, 81–95.

Whitham, G. B. 1974 *Linear and Nonlinear Waves*. Wiley.

Wilson, K. C. 1989 Mobile-bed friction at high shear stress. *J. Hydraul. Engng ASCE* **115**, 825–830.

Zanker, K. J. & Bonnington, S. T. 1967 Recent research development in hydraulic dredging. In *Dredging* (ed. J. T. Williams, G. L. Hargreaves & J. E. G. Palmer) pp. 81–96. Institution of Civil Engineers London.